Petrophysical Studies of Well Cuttings from a Continues Geological Profile in Hockley County, Texas

By:

Tristan Tom

Presented to the Faculty of the Graduate School of

The University of Texas at Arlington in Partial Fulfillment

of the Requirements

for the Degree of

MASTER OF SCIENCE IN EARTH AND ENVIRONMENTAL SCIENCES

THE UNIVERSITY OF TEXAS AT ARLINGTON

December 2021

Abstract

Petrophysical Studies of Well Cuttings from a Continues Geological Profile in Hockley County, Texas

Tristan Tom, MS

The University of Texas at Arlington, 2021

Supervising Professor: Qinhong Hu

The Permian Basin currently leads the oil production in the United States; however, with increasing concerns for the global climate, it is crucial for oil and gas companies to operate as economically and efficiently as possible. This is where the use of well cuttings comes in, as they allow for more geological formations in the subsurface to be analyzed in depth and are cheaper to achieve than core samples. Well cuttings can be obtained from most drilling operations, and they can save on analysis time and even be analyzed on site. Before using well cuttings, it is important to ensure that the well cuttings give a good data and are a viable substitution and supplementation for core samples. This study investigated the viability of well cuttings using various tests of helium pycnometry, enveloping density, X-ray diffraction (XRD), pyrolysis, total organic carbon (TOC), and gas diffusion tests. These integrated tests produced data for petrophysical properties such as particle density, bulk density, porosity, mineralogical content, TOC content, thermal maturity, and gas diffusion coefficient. Well cutting samples were obtained from one well, Spade K in Hockley County, Texas. A total of 12 sample intervals from this well covered a 3340-foot depth range to include five different geologic formations. The testing results of these well cutting samples suggest that particle density, bulk density, thermal maturity, and pyrolysis data can all be obtained from well cutting samples, replacing core samples with current laboratory practices. For X-ray diffraction, more information on drilling fluid is needed, and sample preparation will need to be adjusted but the experimental procedures are adequate. Gas diffusion testing in this study were inconclusive.

Table of Content

List of Figures

List of Tables

List of Abbreviations

cm	Centimeter
ft	Foot
g	Gram
GRI	Gas Research Institute
MIP	Mercury Intrusion Porosimetry
NMR	Nuclear Magnetic Resonance
SK	Spade K well
TOC	Total Organic Carbon
TX	Texas
XRD	X-Ray Diffraction
μm	Micrometer

Acknowledgements

I would like to thank Dr. Qinhong Hu for accepting me into his research group and giving me the opportunity to complete my master's degree, and for all his help and support he has given me along the way. I would also like to thank my committee members Dr. Majie Fan and Dr. John Wickham for their time and support.

I would like to thank Dr. Hu's entire research group for welcoming me into the group and all the help that they gave me along the way. A special thank-you goes to Qiming Wang for all the help and guidance both inside and outside the laboratory. Thanks goes to Thomas Smith who has coordinated with Canan Mowrey Operating about sample donation for this thesis work. I would also like to thank my parents for always supporting me and giving me the best opportunity to succeed in life. Lastly, I would like to thank my partner Sam for always being there for me and for constantly loving and supporting me.

Chapter 1: Introduction

The Permian Basin, which extends form west Texas into southeastern New Mexico, is the top producing oil and gas field in the United States. The Permian Basin has been producing oil and gas for around 100 years and as of 2018 has produced about 33.4 billion barrels of oil and about 118 trillion cubic feet of natural gas (EIA, 2018). Even as the largest oil and gas field in the United States, the production in a single well will commonly start to slow as returns diminish due to multiple factors. It is important for oil and gas companies to save cost while still maximizing drilling efficiency and production. This is where the uses of well cuttings comes in place to characterize the petrophysical properties of subsurface formations.

As fragments of the rock formation being drilled into, well cuttings are grain-sized chips that are a byproduct of most drilling operations. Well cuttings come to the surface during the drilling process and the depth from which they are originated can be recorded. Commonly these cuttings being brought to the surface are no more than a few millimeters in size (Figure 1).

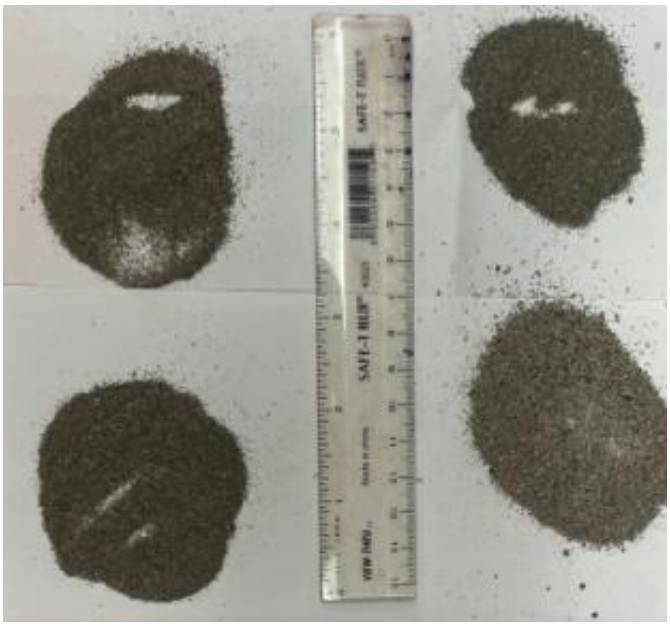

Figure 1: Example of cuttings with each pile representing a 10 ft - interval being collected

Well cuttings were originally thought of as a waste produced from the drilling process, and it was until the 1980's for that opinion to start to change. There were a few papers published in the 1980's suggesting that well cuttings could be useful for well analyses. This has led to more studies looking into the accuracy of data that could be obtained from well cuttings.

In 2000 a paper by Santarelli et al. (2000) stated that they were able to obtain reliable porosity, permeability, and density data by using well cuttings in comparison to core plugs. Another paper by Carreno et al. (2018) used well cuttings to produce data from x-ray diffraction (XRD), helium porosity, and mercury intrusion porosimetry (MIP). The same paper of Carreno et al. (2018) also used the well cuttings to get geochemical data such as total organic carbon (TOC) and pyrolysis. Along with these two studies, there are several more that come up with conclusive data to show that well cuttings could generate good reliable data for reservoir analyses for example: Ahmed et all (2020), Permata et al (2020), Ghosh et al (1985), and Wittman et al (2020).

Since well cuttings are a byproduct of most drilling processes, they are easy and cheap to acquire, unlike cores that can only be acquired by using special drill bits. Cores also take longer to drill and are harder to transport and store due to their size and weight. Cuttings can simply be collected in depth-marked bags or envelops and transported with a normal vehicle rather than an eighteen-wheeler (Figure 1). The work of Carreno et al. (2018) also noted that the analyses of their well cutting samples only took 60 days, when it would have taken 120 days to analyze core samples that covered the same depth interval. It is worth noting that core samples do offer better precision and versatility when running a wider range of tests, which are also more expensive and more time-consuming. Therefore, oil and gas companies have started to use well cuttings to understand rock properties for maximizing petroleum production. The use of well cuttings is

cost-effective by cutting down analytical times and costs, and therefore, allowing for more wells and samples to be analyzed in shorter periods of time for some drilling and production operation decisions to be made. Without using well cuttings, most wells would be drilled and only limited petrophysical data would be collected since it is not practical and feasible to obtain cores from every well. Using well cuttings allows for more data to be collected which helps companies to be more productive economically. This study will give a petrophysical characterization for several formations using well cuttings to provide insights about if the data received from the well cuttings are reliable, in comparison to core data from previous studies.

Chapter 2: Geological Setting

2.1 Study Area and Geological Setting

The Permian Basin is an asymmetrical complex sedimentary system located in west Texas and southeast New Mexico in the foreland of the Marathon-Ouachita orogenic belt (EIA 2020). Approximately 320-325 million years ago in the middle of the Carboniferous period, the Permian Basin was developed in an open marine area called the Tobosa Basin (EIA, 2020). The Tobosa Basin was formed as the result of a structural flexure, at the Sothern margin of the North American plate, in the Precambrian basement during the late Proterozoic. After this formation, sediments were eroded and deposited from the surrounding highlands (Brown et al., 1973; Beaumont, 1981; Jordan, 1981). The Permian Basin today is bordered by the Northwest Shelf and Matador Arch to the north and is composed of three main subdivisions including sub-basins and platforms. These three main subsets of the Permian Basin are the Midland Basin, Delaware Basin, and the Central Platform (EIA, 2020).

The tectonic history of Midland and Delaware Basins is mostly affected by their rapid subsidence due to the uplift of the Central Platform and slight effects of the Marathon-Ouachita orogenic belt (EIA, 2020). The uplift of the Central Platform and the subsidence of the Midland and Delaware Basins took place during the Pennsylvanian and Woflcampian, times as seen in the sudden thickness and lithologic changes of the Pennsylvanian and Permian strata. The subsidence of the Midland and Delaware Basins lasted until the end of the Permian, but the deformation slowed after the Wolfcampian time (EIA, 2020). Once the major tectonic activity subsided, a carbonate shelf was developed around the Midland Basin. The development of the carbonate shelf took place after a siliciclastic sedimentation which started in the early Pennsylvanian (Robinson, 1988). Once the early Leonardian time came, the shelf started to become a distinctly rimmed margin which influenced the depositional environment. This led to the basins being sites of siliciclastic accumulation, while the platforms and shelfs were sites of carbonate deposition (Yang and Dorobek, 1995; EIA, 2020;).

The well Spade K used for this study is between the Midland Basin and the Matador Arch on the Northwest shelf in Hockley County, Texas (Figure 2). The stratigraphy shown in the well log for the Spade K well in this study does not match the general stratigraphy among any of the three main subsets of the Permian Basin (Figure 3), which is to be expected since the well is not located exactly in any of the Permian Basin subsets. Also as expected, the stratigraphy of the well does not exactly match that on the Northwest Self (Figure 4), since it is more in an area that could be considered as the northern shelf. Starting with the shallowest formation and ending with the deepest, the stratigraphic formations of this well are as follows: Glorietta, Upper Clearfork, Clearfork Poros, Dean, Wolfcamp, Wolfcamp Shale, Cisco, Cline, and lastly Strawn (Table 1).

The Formations to be looked at in this study are the Clearfork Poros, Wolfcamp, Woflcamp Shale, Cisco, and Strawn.

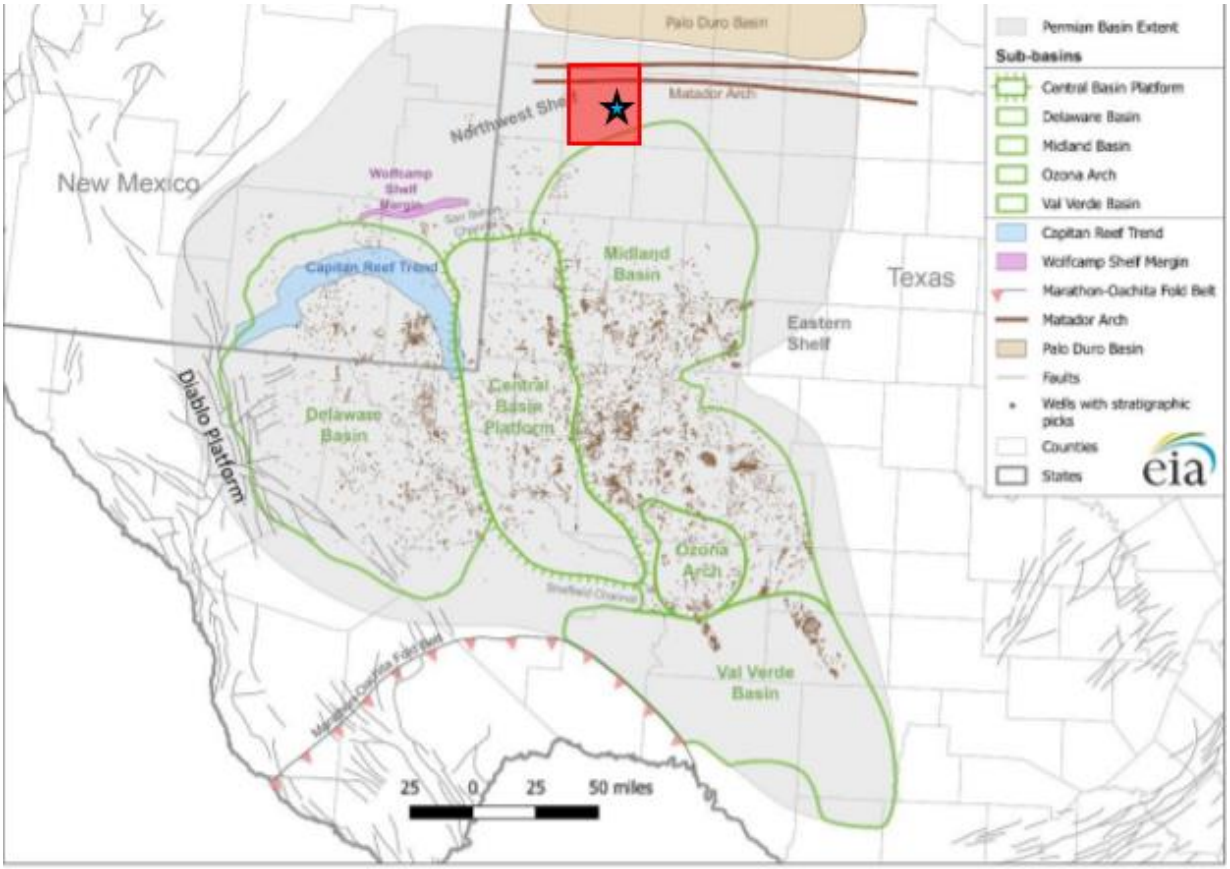

Figure 2: Location of Hockley County (red square), the well for the study (blue star), and the features of the Permian Basin.

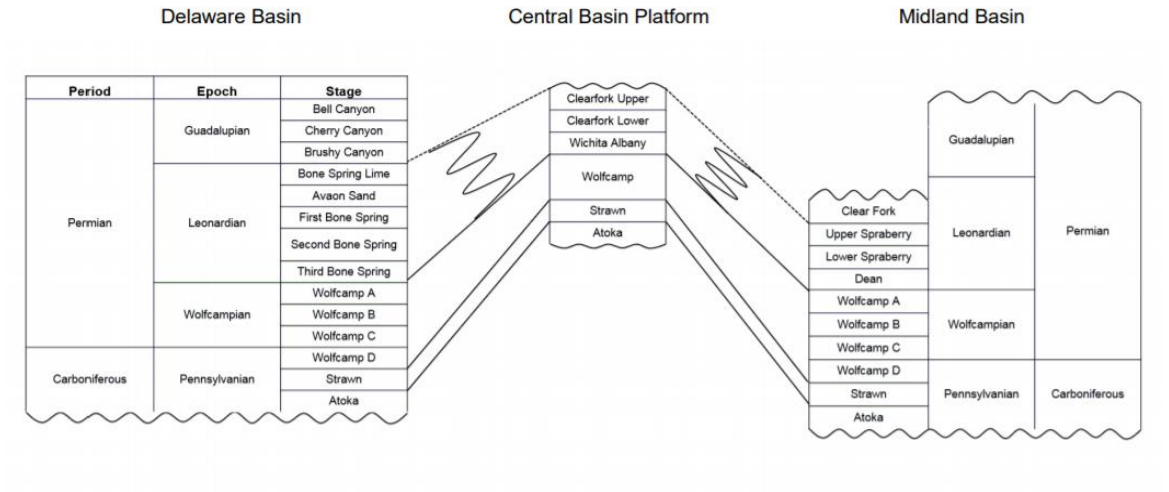

Source: U.S. Energy Information Administration based on DrillingInfo Inc., U.S. Geological Survey.

Figure 3: Stratigraphy of the Central Basin platform compared to the Delaware and Midland Basins.

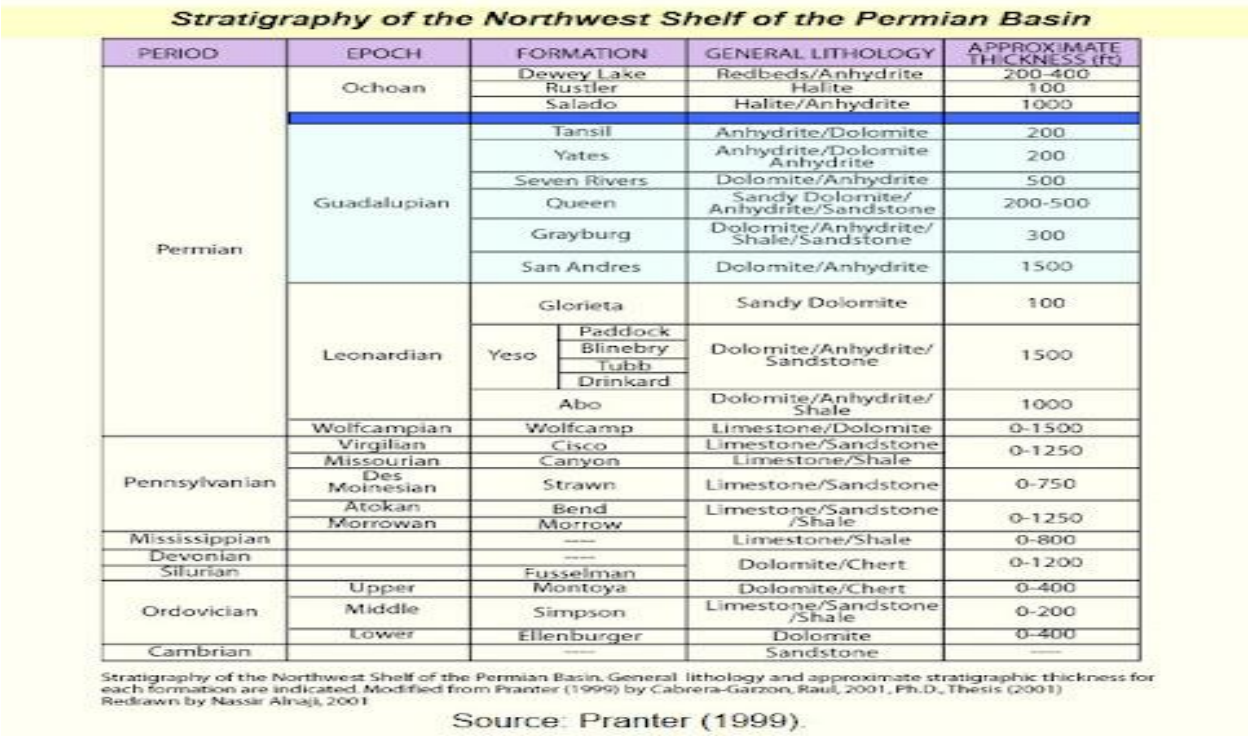

Stratigraphy of the Northwest Shelf of the Permian Basin

PERIOD	EPOCH	FORMATION	GENERAL LITHOLOGY	APPROXIMATE THICKNESS (ft)
Permian	Ochoan	Dewey Lake	Redbeds/Anhydrite	200-400
		Rustler	Halite	100
		Salado	Halite/Anhydrite	1000
	Guadalupian	Tansil	Anhydrite/Dolomite	200
		Yates	Anhydrite/Dolomite Anhydrite	200
		Seven Rivers	Dolomite/Anhydrite	500
		Queen	Sandy Dolomite/ Anhydrite/Sandstone	200-500
		Grayburg	Dolomite/Anhydrite/ Shale/Sandstone	300
		San Andres	Dolomite/Anhydrite	1500
	Leonardian	Glorieta	Sandy Dolomite	100
		Yeso: Paddock, Blinebry, Tubb, Drinkard	Dolomite/Anhydrite/ Sandstone	1500
		Abo	Dolomite/Anhydrite/ Shale	1000
	Wolfcampian	Wolfcamp	Limestone/Dolomite	0-1500
Pennsylvanian	Virgilian	Cisco	Limestone/Sandstone	0-1250
	Missourian	Canyon	Limestone/Shale	
	Des Moinesian	Strawn	Limestone/Sandstone	0-750
	Atokan	Bend	Limestone/Sandstone /Shale	0-1250
	Morrowan	Morrow		
Mississippian		----	Limestone/Shale	0-800
Devonian		----	Dolomite/Chert	0-1200
Silurian		Fusselman		
Ordovician	Upper	Montoya	Dolomite/Chert	0-400
	Middle	Simpson	Limestone/Sandstone /Shale	0-200
	Lower	Ellenburger	Dolomite	0-400
Cambrian		----	Sandstone	----

Stratigraphy of the Northwest Shelf of the Permian Basin. General lithology and approximate stratigraphic thickness for each formation are indicated. Modified from Pranter (1999) by Cabrera-Garzon, Raul, 2001, Ph.D., Thesis (2001) Redrawn by Nassir Alnaji, 2001

Source: Pranter (1999).

Figure 4: Stratigraphy of the Northwest Shelf of the Permian Basin

Table 1: Age and stratigraphic sequence covered in the study well with depths and sample numbers.

Age	Formation	Samples	Depth Range (ft)
Permian	Glorietta		5477- 5747
	Upper Clearfork		5757-6161
	Clearfork Poros	Sk-1,2,3,4, 5	6161-7849
	Dean		7849-8240
	Wolfcamp	Sk-6	8240-8697
	Wolfcamp Shale	Sk-7,8,9	8697-9648
Pennsylvanian	Cisco	Sk-10, 11	9648-9986
	Cline		9986-10038
	Strawn	Sk-12	10038-10250

2.2 Lithologic Units

The Clearfork Poros Formation, also referred to as the lower Clearfork Formation, is positioned under the Upper Clearfork Formation and on top of the Dean Formation. As described by the well log for the Spade K well, the Clearfork Poros starts at the depth of 6161 feet (ft) and ends at 7849 ft (Table 1). The top 559 ft of 1688 ft Clearfork Poros Formation is mostly made up of dolomite with small amounts of chert found at the bottom of this portion. At the 6720 ft mark all the way down to the bottom boundary of the Clearfork Poros, the formation is comprised of an off-white to dark-gray limestone with small intervals of shale mixed in; this section of the Clearfork Poros is where the first five samples of this study are taken from (Table 1). Below the Clearfork Poros is the Dean Formation being made up of shale, limestone, and sandstone. The Dean Formation runs from a depth of 7849 ft to 8240 ft, this formation was not used in this study since it did not have a large enough section of consistent and uniform lithology. At 8240 ft depth, the Wolfcamp Formation starts and runs down to the depth of 8697 ft. This formation is made up of medium-gray limestone with intervals of medium-to-dark gray shale mixed in, there is one sample taken from this formation (Table 1). At the 8697 ft depth mark, the next member of the

Wolfcamp Formation starts, referred to in the well log as the Wolfcamp Shale. The Wolfcamp Shale runs down to the Cisco Formation boundary at 9648 ft. The Wolfcamp Shale is composed of a dark shale with light-to-medium gray limestone mixed in from the upper boundary depth of 8697 ft until 9130 ft deep. At 9130 ft, the formation is all dark-gray shale for 230 ft until a depth of 9360 ft. At 9360 ft there is a 140 ft section of light gray sandstone to a depth of 9500 ft. From 9500 ft to the formation boundary at 9648 ft, the Wolfcamp Shale is once again completely dark-gray shale. Three samples for this study are taken form the Wolfcamp Shale, all within the full shale intervals (i.e., no sandstone sample from the depth interval of 9360-9500 ft) (Table 1).

The Cisco Formation stats at a depth of 9648 ft and runs to the Cline Formation boundary at 9986 ft. The upper 252 ft of the Cisco Formation is a medium-gray shale. The Cisco Formation transitions into a dark-gray shale at 9900 ft and stays that way until the Cline boundary at 9986 ft. Two samples were taken from the Cisco Formation, with one from the medium-gray shale section and another from the dark-gray shale sections. The Cline Formation is a small 52 ft thick formation that stars at 9986 ft and ends at 10038 ft where the Strawn Formation starts. It is made up of limestone, light shale, and dark shale. The Strawn Formation starts at 10038 ft deep and runs past the end of the well at 10250 ft. The Strawn Formation is mostly limestone with small amounts of shale and dolomite, there is one sample taken from this formation being used in this study (Table 1).

Chapter 3: Methodology

3.1 Sample Acquisition and Preparation

Cuttings samples from Spade K well, located in Hockley County, Texas, were acquired from Canan Mowrey Operating. Since the samples from this study are from the same well, they make a continuous vertical profile. The well cuttings samples came in envelopes marked for every 10 ft of depth (Figure 5). Each 10 ft interval envelope contained about 5 grams (g) of sample and ideally about 100 g is required for various laboratory tests with additional sample mass being preferred. To ensure that there is enough sample for testing, 7 to 20 of the 10 ft intervals were combined to result in 12 samples that cover 70 to 200 ft intervals. To make sure that there was not too much lithologic variation within the sample's interval, the well log was carefully examined. When looking at the well log, sample intervals were determined based on lithology. The samples intervals were chosen only if they contained a constant lithologic profile. Therefore, within the sample interval there is mostly one lithology with little to no major lithologic variations. Throughout the vertical profile, there were 12 sections that meet this criterion and were large enough (70 ft or more) to run tests on.

A)

B)

C)

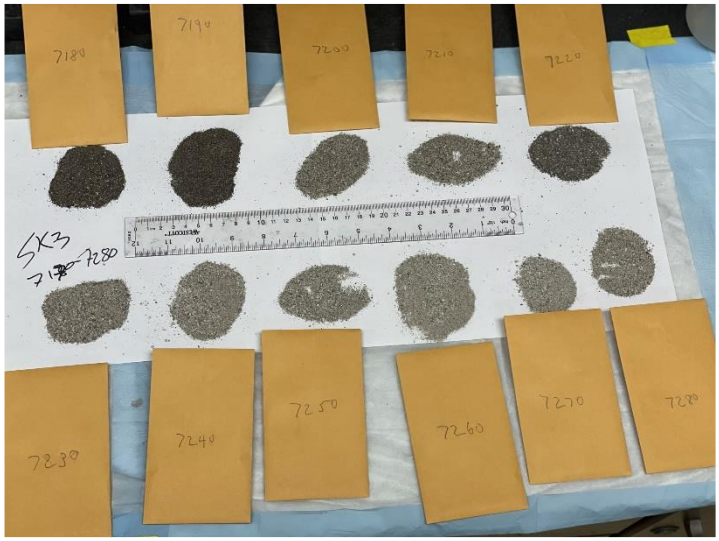

D)


SK-4
7580'-
7710'

E)

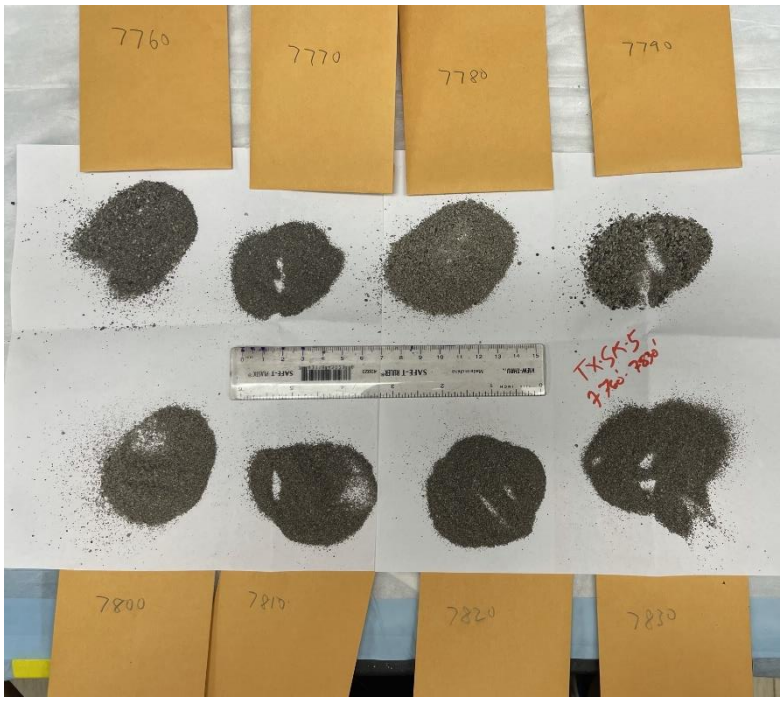
7760
7770
7780
7790
TX-SK-5
7740'-7830'
7800
7810
7820
7830

F)

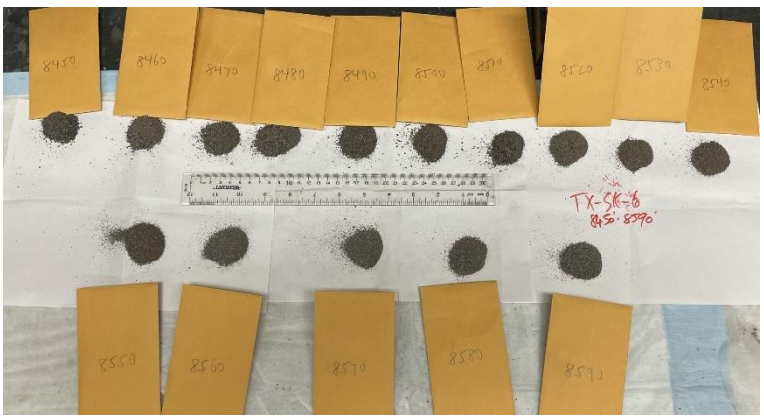
TX-SK-6
8450-8590'

G)

H)

I)

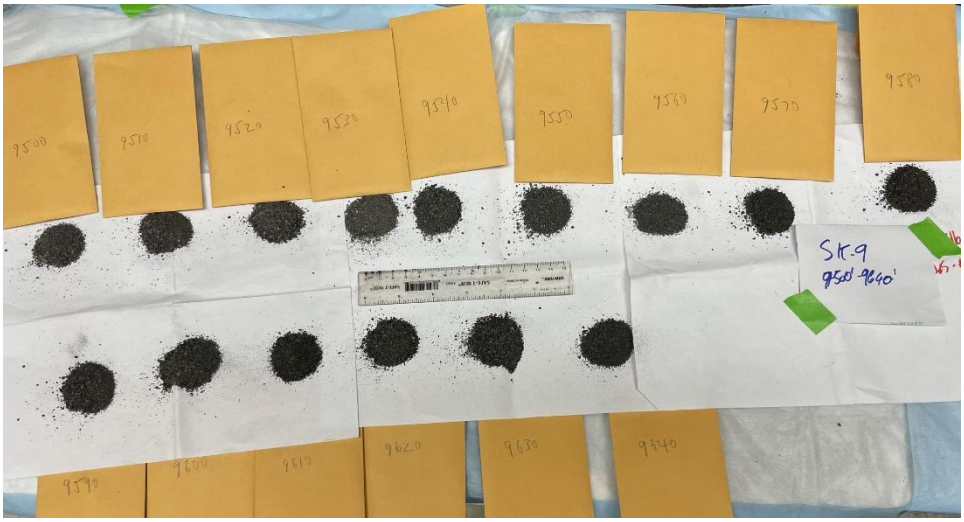

J)

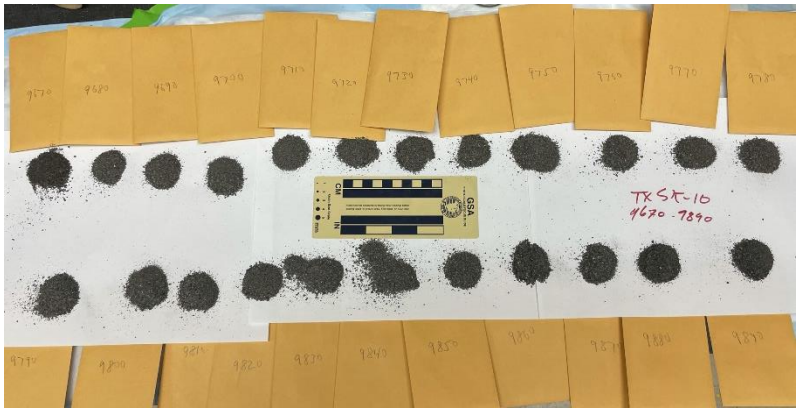

K)

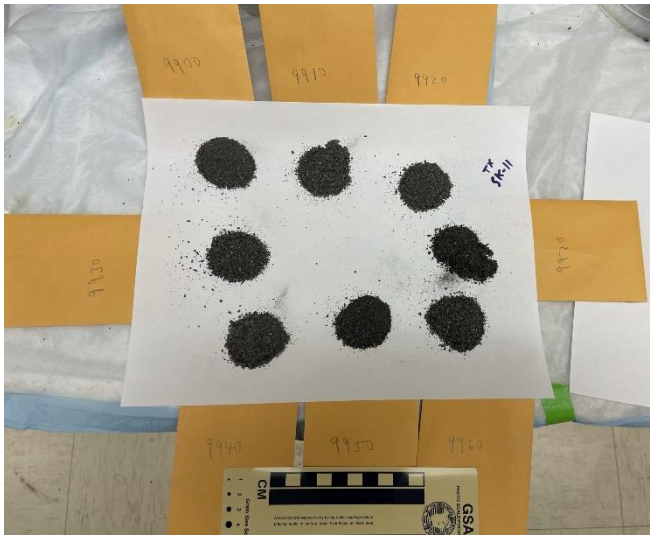

L)

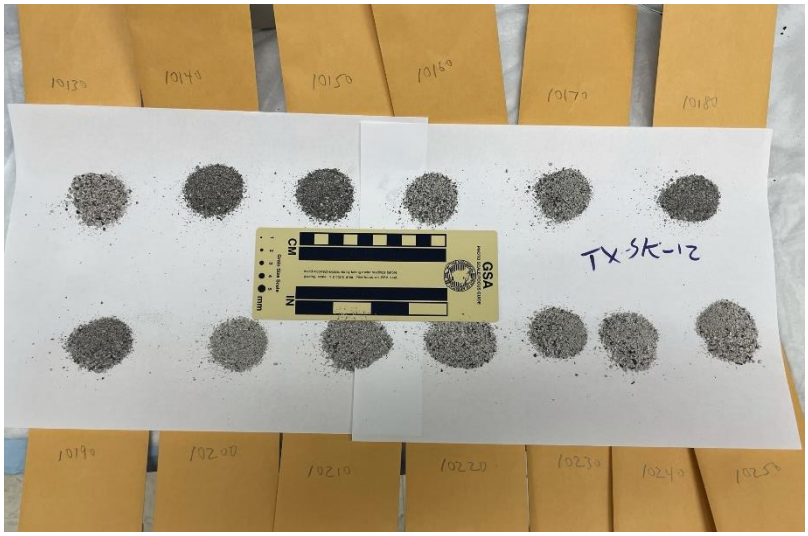

Figure 5: (A-L) View of the well cutting samples used in this study; TX: Texas, SK: Spade K well

After sample intervals were determined, the 7 to 20 10-ft interval envelopes were poured out next to each other to ensure that there was no visible variation in lithology by looking at the color of each pile (Figure 5). Next, the 10 ft interval piles were sorted through to remove any impurities such as plastic or fibers. The samples were then photographed and combined. After the 7 to 20 10-ft interval envelops were combined to make 70 to 200 ft intervals, the samples were then run through a series of sieves (Figure 6). The sieves split the samples into 5 granular size intervals, termed as Sizes (with a decreasing grain size) A, GRI, B, C, and Powder. Size A represents grains from 841 to 1700 micrometers (μm); Size GRI (Gas Research Institute) is composed of grains from 500 to 841 μm; Size B is 177 to 500 μm; Size C is 75 to 177 μm; and Powder represents grains smaller than 75 μm. The samples were split into different granular sizes for a couple of reasons: first, it tells us the proportion of grain sizes in the well cuttings samples; second, different-sized granular samples are used for different analytical experiments.

While the samples were still in the sieves, water was run through to ensure that any soluble impurities were washed off and that the grains settled to the proper sieve. After the samples were washed, they were transferred to a 60-degree Celsius oven to dry. Once the samples were dried, they were removed from the sieves and transferred into containers based on grain sizes to await testing. Table 2 below shows all samples, their depth ranges, formation lithology, and total mass. Table 3 shows the mass distribution of each size of sample. Since the samples for this study are well cuttings and each sample covers a depth range of 70 to 200 ft, all resultant data will represent an average of these depth intervals.

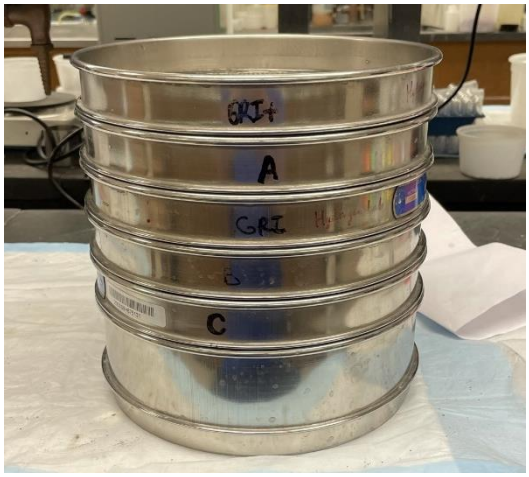

Figure 6: Sieve stack used to separate samples into different granular sizes

Table 2: Samples, depth interval, Formation, lithology, and total mass

Sample Name	Depth Range (ft)	Formation	Lithology	Total Mass (g)
Sk-1	6910-7070	Clearfork Poros	Limestone	74.1
Sk-2	7080-7170			49
Sk-3	7180-7280			57.9
Sk-4	7540-7710			92.5
Sk-5	7760-7830			35.5
Sk-6	8450-8590	Wolfcamp	Limestone	69.5
Sk-7	8740-8970	Wolfcamp Shale	Shale	106.4
Sk-8	9130-9360			132.4
Sk-9	9500-9640			72.9
Sk-10	9670-9890	Cisco	Shale	128.8
Sk-11	9900-9970			37.2
Sk-12	10130-10250	Strawn	Limestone	62.4

Table 3: Grain size mass distribution of each sample

Sample Name	Total Sample Mass (g)	Size A Mass (g)	Size GRI Mass (g)	Size B Mass (g)	Size C Mass (g)	Powder Mass (g)
Sk-1	74.1	0.3	3.9	50.1	18.8	1.3
Sk-2	49	4.1	9.3	28.3	6	1.3
Sk-3	57.9	4.8	12.2	31.9	5.1	3.9
Sk-4	92.5	11	21.4	50.2	6.9	3
Sk-5	35.5	1.7	2.6	19.7	8.1	3.4
Sk-6	69.5	4.9	9.4	42.9	7.8	4.5
Sk-7	106.4	3.2	6.7	80.8	11.9	3.8
Sk-8	132.4	24.4	24.6	52.9	16.6	13.9
Sk-9	72.9	20.1	22.4	23.6	2.1	4.7
Sk-10	128.8	37.4	36.6	43.3	4.5	7
Sk-11	36.7	2.4	7.8	19.9	2.3	4.3
Sk-12	62.9	3.5	15.3	32.5	6.4	5.2

3.2 Particle Density

A Micromeritics helium gas pycnometer was used to determine the particle density of 12 samples. Particle density data was collected for every granular size (Sizes A, GRI, B, and C) for each sample. The process of measuring particle density started with drying the sample at 60-degree Celsius for two days. Then the sample was weighed and placed into one of the air-tight sample chambers with a known volume; the choice of sample chamber depends upon the sample mass available. This chamber was then placed into the Micromeritics AccuPyc II 1340 instrument (Figure 7); the instrument purged the chamber with helium, then emptied and refilled with helium. The instrument tracked the amount of helium in the sample chamber and used the known volume of the sample chamber with the manually entered sample mass to produce particle density results. The test was run five times to produce the result of average and standard deviation.

Figure 7: Micromeritics AccuPyc II 1340 with two different-sized sample chambers

3.3 Bulk Density

Bulk density data were collected using a Micromeritics GeoPyc 1365 (Figure 8), and Sizes A, GRI, and B size samples were used for this experiment. When using the GeoPyc instrument with granular sizes GRI or smaller, non-porous quartz powder must replace the typical enveloping material, DryFlo^{TM} (Zhao et al., 2021). To get bulk density data for GRI and B sized grains using the instrument, the packing pore of GRI and B grains must be determined. This was achieved by putting a weighed-out amount of quartz powder, of the corresponding size (i.e., GRI or B), into the GeoPyc's sample tube (Figure 8). The solid granular quartz "standards", at the same sizes as the granular cutting samples, were crushed from quartz crystals of several cm in size from Godfrey of Ontario in Canada obtained from Ward's Science. The sample tube

was then placed into the instrument and compacted at 38 N to ensure a close contact of the enveloping materials (quartz powder or DryFlo^{TM}) and samples to give the total volume. This total volume was used to determine the pore packing volume of the GRI or B sized grains, by using the known density of quartz and the weight of sample taken prior to being emplaced into the tube. This process was repeated three times to evaluate the experimental uncertainty. After the packing pore volume was known, the weighted GRI or size B sample was placed into the sample tube with a weighed amount of quartz powder used as the enveloping material. The tube was then placed into the instrument and compacted. The resultant total volume was used to determine the bulk density. The pore packing volume plus the volume of the quartz powder was subtracted from the total volume to obtain the volume of the GRI- or B-sized sample; this volume was then used with the recorded sample mass to calculate the bulk density of granular samples (Zhao et al., 2021).

The equations used to acquire bulk density using the quartz packing pore method are as follows:

Equation for packing pore: $v_{pp} = v_t - v_q$

Equation for quartz volume: $v_q = m_q / \rho_q$

Equation for bulk density: $\rho_b = m/v$

Equation for sample volume: $v = v_T - v_{pp} - v_q$

v_{pp}: volume of packing pore of the granular size in use, cm^3

v_t: total volume measured by the instrument, cm^3

v_q: total volume of quartz, cm^3

m_q: mass of quartz used, g

ρ_q: density of quartz (2.65 g/cm^3), g/cm^3

ρ_b: bulk density of the sample, g/cm^3

m: mass of the sample, g

v: volume of the sample, cm^3 ρ

For Size A samples with the large granular size, the quartz powder method is not necessary and DryFlo™ can be used as the enveloping material. The methodology for using DryFlo™ differs from the quartz powder method. First, the DryFlo™ was placed into the cylindrical sample chamber and put in the Micromeritics GeoPyc 1365 to be run as a blank; this allows the volume of the DryFlo™ to be calculated. After the blank test was run, the sample was weighed and added into the sample chamber; this was then placed in the instrument and compacted. The instrument used the input mass of the sample and the envelope volume to derive a bulk density.

Figure 8: Micromeritics GeoPyc 1365 and a cylinder-shaped sample chamber

3.4 X-Ray Diffraction (XRD)

XRD was used to determine the mineralogical composition and contents of each sample, using the Powder-sized fraction. The XRD instrument used was a Shimadzu MaximaX XRD-

7000 X-ray Diffractometer (Figure 9), which measures the intensities and angles of the x-ray beams diffracted by the mineral crystals in the sample. To run this test, powder samples were placed into the sample holder, and then compacted down to fit in the holder with as flat and smooth of a surface as possible. The sample was then placed onto the analysis stage and the scanning conditions were set. The XRD analysis was run, and data were received for mineralogy identification and analyzed using Jada 9 software to determine the percentage of whole mineralogic composition. The step-by-step process of XRD analyses can be found in Appendix A.

Figure 9: Shimadzu MaximaX XRD-7000 X-ray Diffractometer

3.5 Pyrolysis and Total Organic Carbon (TOC)

Pyrolysis data were gathered by GeoMark Research, with about 100 milligrams of powder sample using the Rock Eval or HAWK pyrolysis instrument. Pyrolysis data were used to help understand the thermal maturities of the samples compared to past studies to ensure cutting samples are a viable substitute for core samples.

TOC contents were also analyzed with the powder-sized sample by GeoMark Research with the LECO C230 instrument. This instrument requires the initial decarbonization by treating the sample with hydrochloric acid (HCl). Then the sample was dried and run through a filter before it was placed in the instrument. Once being placed in the instrument the sample was combusted, and the TOC data were collected. The data were used to corollate with the other petrophysical data and determine thermal maturity of the samples. The full procedure performed at GeoMark for TOC and pyrolysis can be found in Appendix B.

3.6 Gas Diffusion

Gas diffusion tests were run to determine how gas permeates though the grain-sized samples. This was done with a gas diffusion set up published by Peng et al. (2012) (Figure 10). This test yields oxygen diffusion data to understand how the oxygen tracer gas can travel through a vertical profile of different lithologies.

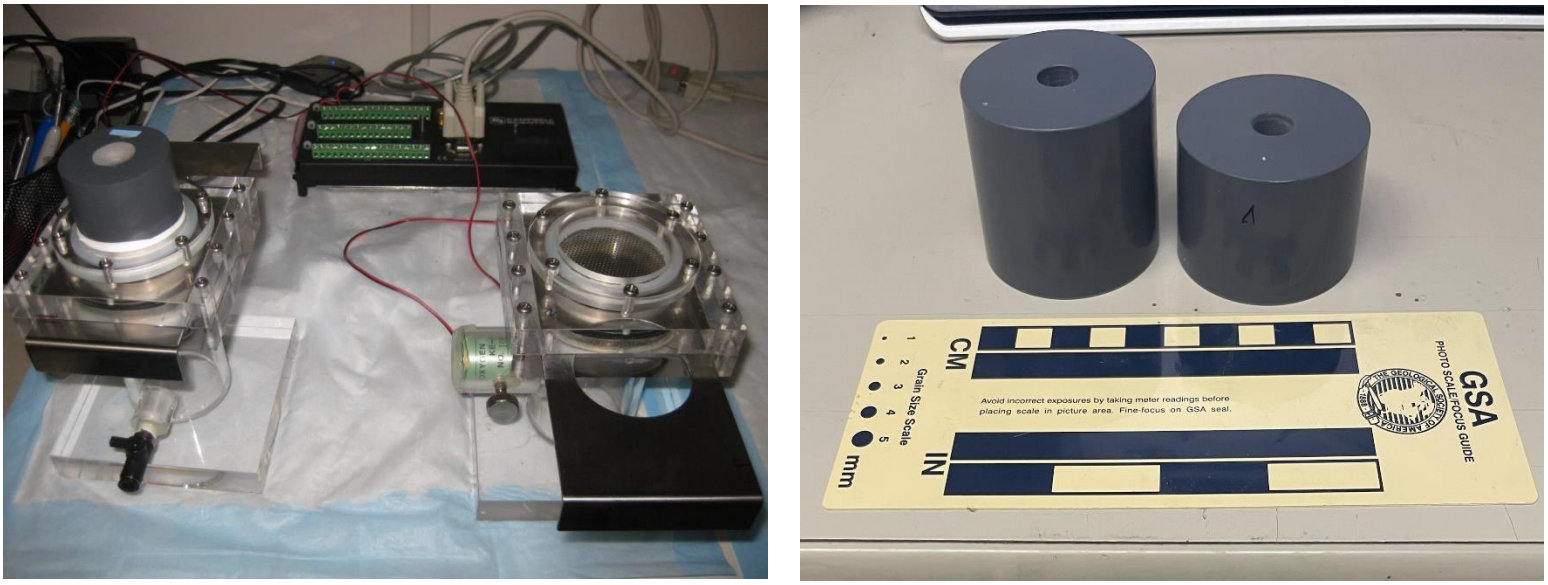

Figure 10: (Left): Gas diffusion set up with a sample chamber at the top and sensor chamber at the bottom. (Right): Sample chambers used: 4cm height on left, 3cm height on right.

Prior to experimentation, samples were dried in a 60-degree Celsius oven. This experiment was completed with Size B samples, as they mostly have the largest portion of the sample (Table 3). Once the samples were dry, a sample chamber was selected (right figure of Figure 10); two sample chambers with different heights were used so both analysis chambers could be used at the same time. Both sample chambers had an inner diameter of 1.1cm; the heights of the chambers were the only thing that was different, one being 3 cm tall and the other 4 cm tall. After selecting the sample chambers, they were placed onto a metal plate and weighed on a balance. Since the chambers have holes at both ends, a metal plate is used to keep the sample in the chamber. Once the chamber and plate were measured on the balance, the balance was zeroed, and the sample was inserted into the chamber until it was flush with the top of chamber. The sample in the chamber was then weighed to record the sample mass, after which the sample and chamber were brough to the gas diffusion setup. A filter paper was placed on the top of sensor chamber, so no samples fall into the sensor chamber of the gas diffusion set-up (left figure of Figure 10). Once the filter paper was placed, the sensor chamber was inverted and

attached to the sample chamber. The sensor chamber was then inverted back upright. The metal plate keeping the sample in the sample chamber could then be removed. Prior to starting the experiment, a metal divider closes the sensor chamber from the sample chamber so there is no communication of the oxygen tracer in the atmosphere (Figure 10). With the sensor chamber closed to the sample chamber the sensor chamber valves were opened. The chamber was then filled with nitrogen gas until the oxygen sensor reads a value of around 0.3 millivolts (mV). Once this background level was reached, the valves to the chamber were closed and the sensor chamber was opened to the sample chamber by sliding the metal divider. This was the start of the experiment while the oxygen sensor voltage and time were recorded. The experiment was left to run with the voltage sensor taking measurements every minute. The experiment was run until the voltage sensor reached about 15 mV. The data collected by the sensor were then imported to an Excel sheet for processing, following the methodologies outlined in Peng et al. (2012).

3.7 Porosity

Porosity was gathered by using the two-density method of particle and bulk densities individually and independently measured (Zhao et al., 2021). Both bulk and particle densities were collected as previously discussed, which are then inputted to the equation below to get porosity:

$$\Phi = 1 - (\rho_b/\rho_p) \times 100$$

Φ: Porosity, as a precent

ρ_b: Bulk density, g/cm^3

ρ_p: Particle density, g/cm^3

Chapter 4: Results

4.1 Particle Density

Particle density data were gathered using the Micromeritics AccuPyc II 1340, and the results for granular Sizes GRI, A, B and C are shown in Table 4. The data collected show that, apart from samples Sk-1, 10, and 12, all other samples show an increase in particle density between Sizes A and C. It is not certain whether Sk-11 shows this exact trend, but Sk-11 does present a particle density increase from Sizes A to GRI (Figure 11).

Table 4: Results of particle density

Sample	Formation	Lithology	Size Designation	Particle Density (g/cm^3); average ± standard deviation
Sk-1	Clearfork Poros	Limestone	A	N/A
			GRI	2.733±0.004
			B	2.652±0.003
			C	2.661±0.009
Sk-2	Clearfork Poros	Limestone	A	2.666±0.002
			GRI	2.654±0.030
			B	2.678±0.002
			C	2.696±0.020
Sk-3	Clearfork Poros	Limestone	A	2.684±0.004
			GRI	2.678±0.006
			B	2.668±0.007
			C	2.731±0.002
Sk-4	Clearfork Poros	Limestone	A	2.632±0.007
			GRI	2.637±0.003
			B	2.707±0.001
			C	2.749±0.005
Sk-5	Clearfork Poros	Limestone	A	2.639±0.004
			GRI	2.613±0.001
			B	2.640±0.002
			C	2.709±0.002
Sk-6	Wolfcamp	Limestone	A	2.603±0.001
			GRI	2.691±0.002
			B	2.664±0.001

			C	2.668±0.002
Sk-7	Wolfcamp Shale	Shale	A	2.542±0.002
			GRI	2.647±0.001
			B	2.598±0.001
			C	2.632±0.001
Sk-8	Wolfcamp Shale	Shale	A	2.565±0.002
			GRI	2.588±0.002
			B	2.610±0.001
			C	2.607±0.003
Sk-9	Wolfcamp Shale	Shale	A	2.576±0.002
			GRI	2.658±0.001
			B	2.608±0.001
			C	2.635±0.002
Sk-10	Cisco	Shale	A	2.728±0.002
			GRI	2.739±0.003
			B	2.743±0.001
			C	2.714±0.002
Sk-11	Cisco	Shale	A	2.627±0.002
			GRI	2.707±0.003
			B	2.639±0.040
			C	2.639±0.001
Sk-12	Strawn	Limestone	A	2.743±0.002
			GRI	2.738±0.001
			B	2.690±0.001
			C	2.687±0.020

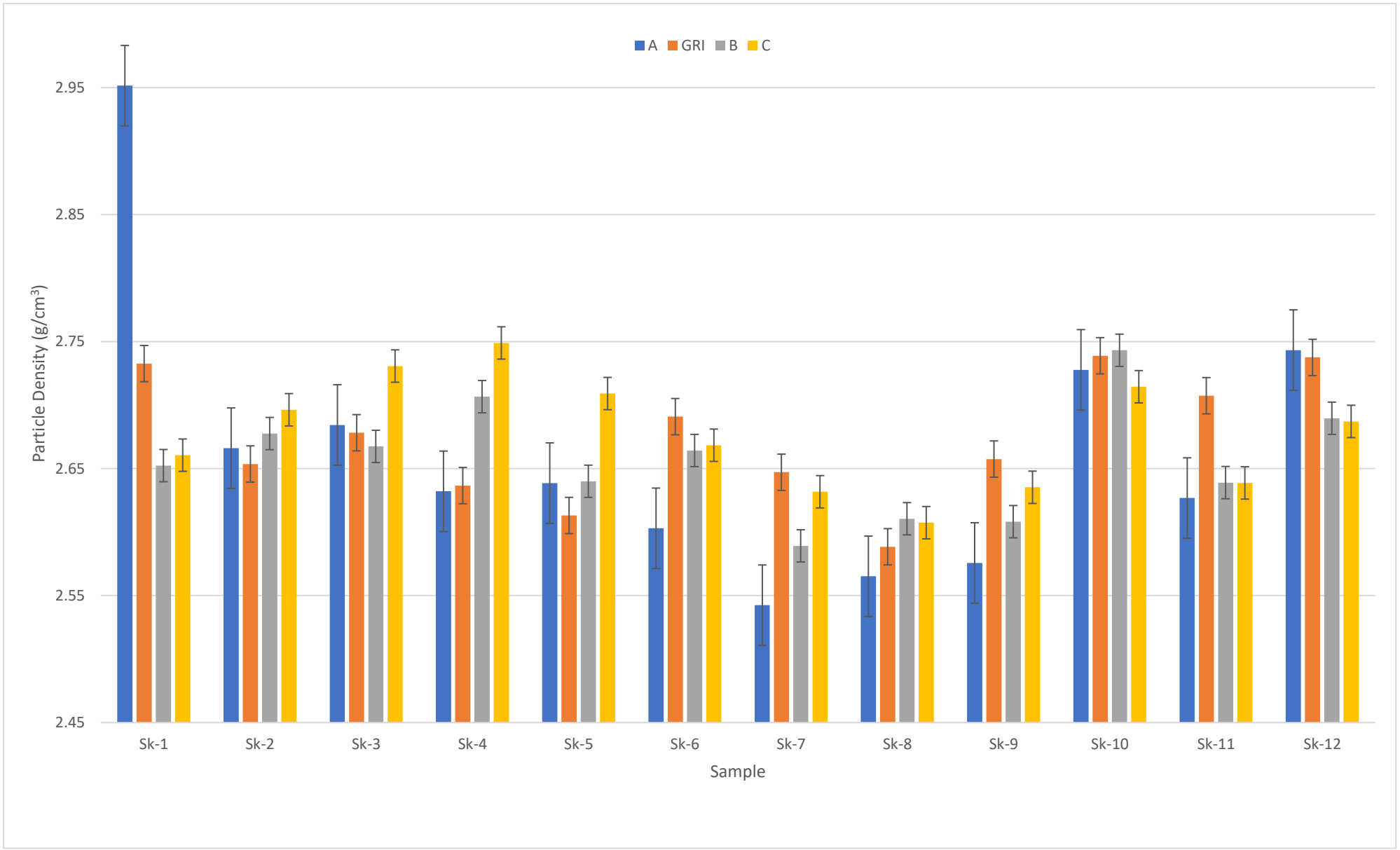

Figure 11: Particle density results by granular sizes with error bars

4.2 Bulk Density

Bulk density data were collected from Micromeritics GeoPyc 1365 using both DryFlo™ and quartz powder methods. All results are shown in Table 5 and depicted in Figure 13. As seen in Figure 12 the shale samples (Sk-7 to Sk-11) show an increase in bulk density for the Size GRI samples. Limestone sample Sk-12 also shows this increase in density for GRI-sized sample. The Clearfork Poros samples (Sk-1 to Sk-5) show an increase in density between sample Sizes A and B.

Table 5: Result of bulk density

Sample	Size Designation	Bulk Density (g/cm^3); average ± standard deviation
Sk-1	A	2.007±0.041
	GRI	2.080±0.086
	B	2.133±0.261
Sk-2	A	2.054±0.039
	GRI	1.956±0.119
	B	2.100±0.123
Sk-3	A	2.121±0.017
	GRI	2.150±0.013
	B	2.204±0.144
Sk-4	A	2.230±0.009
	GRI	2.118±0.035
	B	2.347±0.088
Sk-5	A	2.228±0.005
	GRI	2.080±0.040
	B	2.230±0.017
Sk-6	A	2.205±0.012
	GRI	2.127±0.605
	B	2.022±0.027
Sk-7	A	2.021±0.056
	GRI	2.464±0.162
	B	2.178±0.033
Sk-8	A	2.045±0.009
	GRI	2.389±0.088
	B	2.073±0.170
Sk-9	A	2.035±0.062
	GRI	2.419±0.194
	B	2.018±0.122
Sk-10	A	2.266±0.020
	GRI	2.731±0.145

	B	2.238±0.068
Sk-11	A	2.197±0.048
	GRI	2.513±0.070
	B	2.223±0.063
Sk-12	A	2.199±0.033
	GRI	2.701±0.106
	B	1.954±0.095

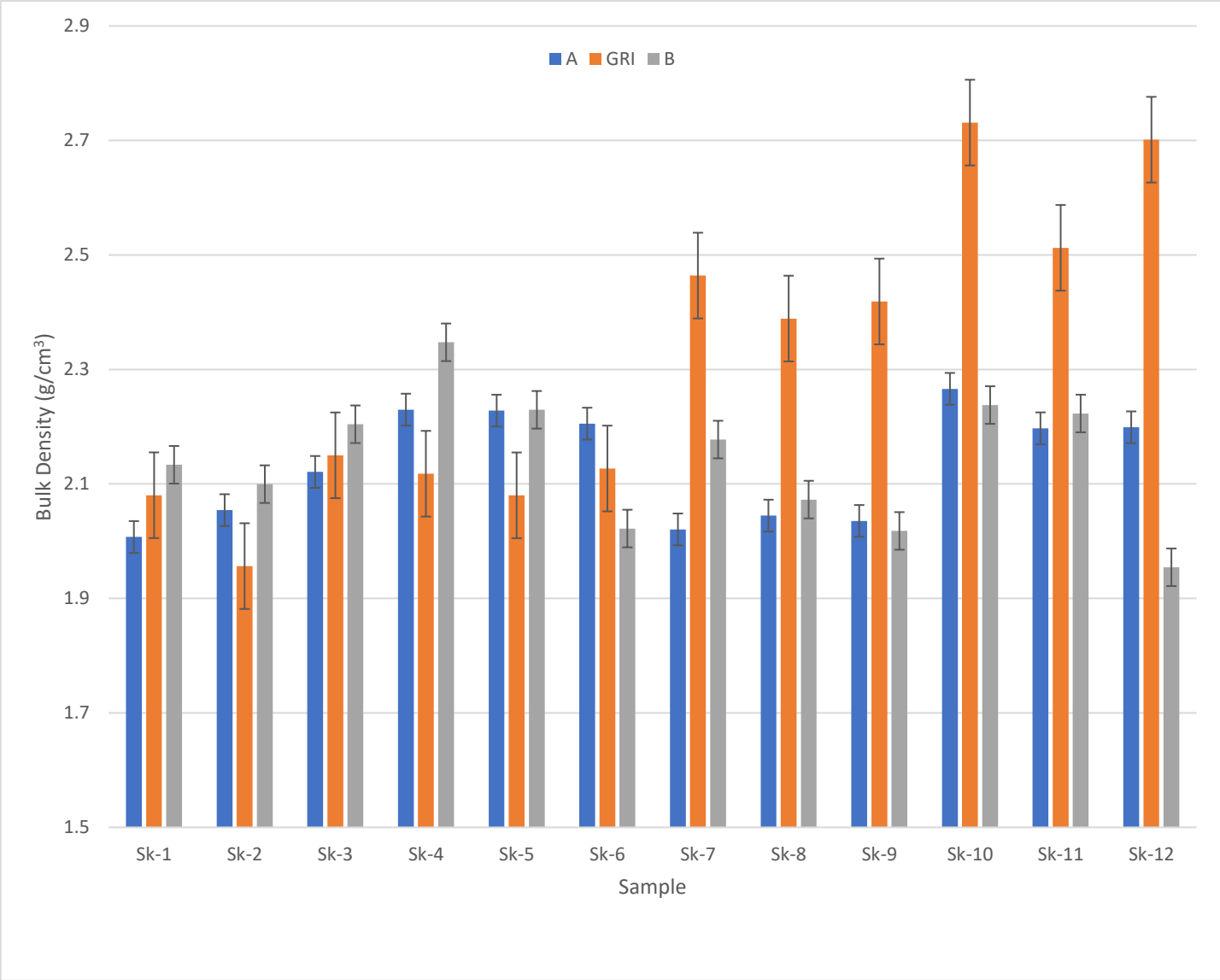

Figure 12: Bulk density results by granular sizes with error bars

4.3 X-ray Diffraction

All XRD results are shown in Table 6 and mineralogical composition by mineral group is shown in Figure 13. Maximum compositions of quartz plus feldspar composition are seen in Sample Sk-8 with 55.4% composition, while Sk-4 has the least with 4.1% composition. Sample Sk-3 has the highest carbonate composition at 91.4% and Sample Sk-10 has the lowest at 9.8%. All samples have a small amount of sulfate minerals to be present, making up 0.2% (Sk-2) to 3.9% (Sk-1, 8-9) of total composition. Clay minerals are observed to vary from up to 38.1% of composition in Sk-10 to as low as 1.7% composition in Sk-3. Samples Sk-7 and -9 have a small amount of other minerals such as halite and analcite. Shale samples (Sk-7 to11) have a higher composition of quartz plus feldspar and clay compositions. As expected, carbonate samples (Sk-1 through 6 and -12) have higher carbonate percentages. None of the shale samples have any dolomite, and all carbonate samples except for Sk-12 have a percentage of dolomite to be present; samples Sk-1 and -3 have the highest amounts of dolomite composition. Ankerite is only present in the shale samples and Sk-12.

Table 6: Mineralogical data by precent composition for each sample

Sample	Composition											
	Quartz	Orthoclase	Plagioclase	Calcite	Dolomite	Ankerite	Siderite	Anhydrite	Pyrite	Clays	Halite	Analcite
Sk-1	14.6	0.5	0.4	61.5	15.2	0	0	2.4	1.5	3.9	0	0
Sk-2	11.4	0	0	81.5	4.2	0	0	0.2	0	2.7	0	0
Sk-3	6.3	0	0	75.5	15.9	0	0	0.6	0	1.7	0	0
Sk-4	4.1	0	0	86.3	4.8	0	0	0.8	0	4	0	0
Sk-5	7	0	0	83.2	6.4	0	0	0.5	0	2.9	0	0
Sk-6	12.8	0	0	74.8	6.5	0	0	0.3	1.3	4.3	0	0
Sk-7	42.7	0	4.7	7.2	0	23.1	0	0.7	3.1	17.9	0.6	0
Sk-8	47.7	0	7.7	9	0	10.2	0	1.1	2.8	21.5	0	0
Sk-9	29.7	0	5.9	12.3	0	16	0	1.1	2.8	32	0	0.2
Sk-10	35.4	0	15.4	4.5	0	0	5.3	1.3	0	38.1	0	0
Sk-11	34.7	0	5.7	26	0	7.7	0	1.6	1.9	22.4	0	0
Sk-12	5.2	0.3	0.7	61.9	0	28.3	0	0.3	0.7	2.6	0	0

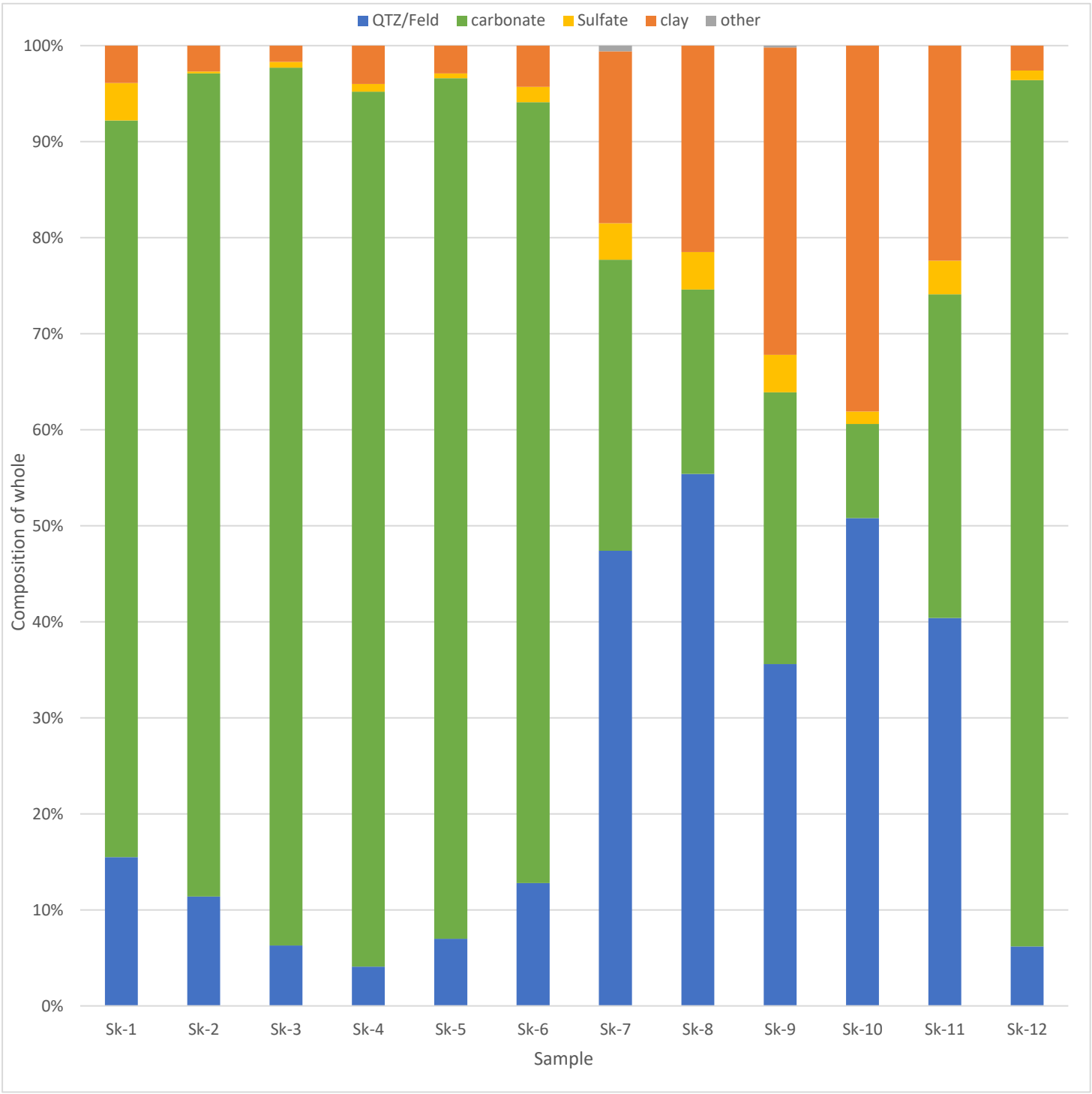

Figure 13: Mineralogical data by mineral groups

4.4 Pyrolysis and Total Organic Carbon

Both pyrolysis and TOC tests were performed by GeoMark Research. These tests yield TOC data with the shale samples having higher TOC and lower carbonate contents. The limestone samples are seen to have much higher oxygen index values than the shales except for Samples Sk-1 and -10. The shale samples also have higher S3 (organic carbon dioxide yield) than the limestone samples apart from Sk-1. As shown in Table 7 for all samples, Sample Sk-8 has the highest TOC content (2.78%), while Sk-4 has the highest carbonate composition at 95.94%. The lowest TOC sample is Sk-12 at 0.27 % and the lowest carbonate percentage is Sample Sk-10 at 20.32%. Sk-7 has the highest S1 value at 1.17 g hydrocarbons/g sample, while Sk-1 has the highest S2 value at 18.93 followed by Sk-7 at 12.21. Sk-1 has a hydrogen index more than 2 times greater than any other samples.

Looking at the plots of the TOC and pyrolysis data (Figures 14-23), all but two of the samples are classified as Type 2 kerogen. All samples are either in the oil generation zone or immature when looking at the production index chart (Figure 17). However, the vitrinite reflectance plot (Figure 18) put all samples in the oil generation window. Figure 16 shows an inverse relationship between carbonate composition and TOC. Figure 14 shows that samples Sk-1, 7-9, and 11 all have good-to-excellent oil potential based on S2 results.

Table 7: Pyrolysis and TOC data

Sample ID	Percent Carbonate (wt.%)	TOC (wt.%)	S1 (mg HC/g)	S2 (mg HC/g)	S3 (mg CO_2/g)	Tmax (°C)	Calculated %Ro (RE TMAX)	Hydrogen Index (S2 x 100/TOC)	Oxygen Index (S3 x 100/TOC)	S2/S3 Conc. (mg HC/mg CO2)	S1/TOC Normalized Oil Content	Production Index (S1/(S1+S2)
Sk-1	79.94	1.83	0.83	18.93	1.34	446	0.87	1,034	73	14	45	0.04
Sk-2	88.66	0.79	0.57	3.21	0.88	446	0.87	409	112	4	73	0.15
Sk-3	95.42	0.38	0.31	1.34	0.83	435	0.67	353	218	2	82	0.19
Sk-4	95.94	0.39	0.29	1.24	0.97	440	0.76	320	250	1	75	0.19
Sk-5	91.32	0.58	0.38	2.03	0.90	436	0.69	353	157	2	66	0.16
Sk-6	81.98	1.25	0.96	4.70	0.86	435	0.67	376	69	5	77	0.17
Sk-7	37.89	2.77	1.17	12.21	0.75	433	0.63	441	27	16	42	0.09
Sk-8	24.66	2.78	0.63	9.12	0.82	436	0.69	328	29	11	23	0.06
Sk-9	36.69	2.56	0.85	9.61	0.49	437	0.71	375	19	20	33	0.08
Sk-10	20.32	1.01	0.25	1.55	2.49	445	0.85	153	247	1	25	0.14
Sk-11	35.37	1.96	0.56	6.26	0.54	439	0.74	319	28	12	29	0.08
Sk-12	88.32	0.27	0.14	0.92	0.75	437	0.71	337	275	1	51	0.13

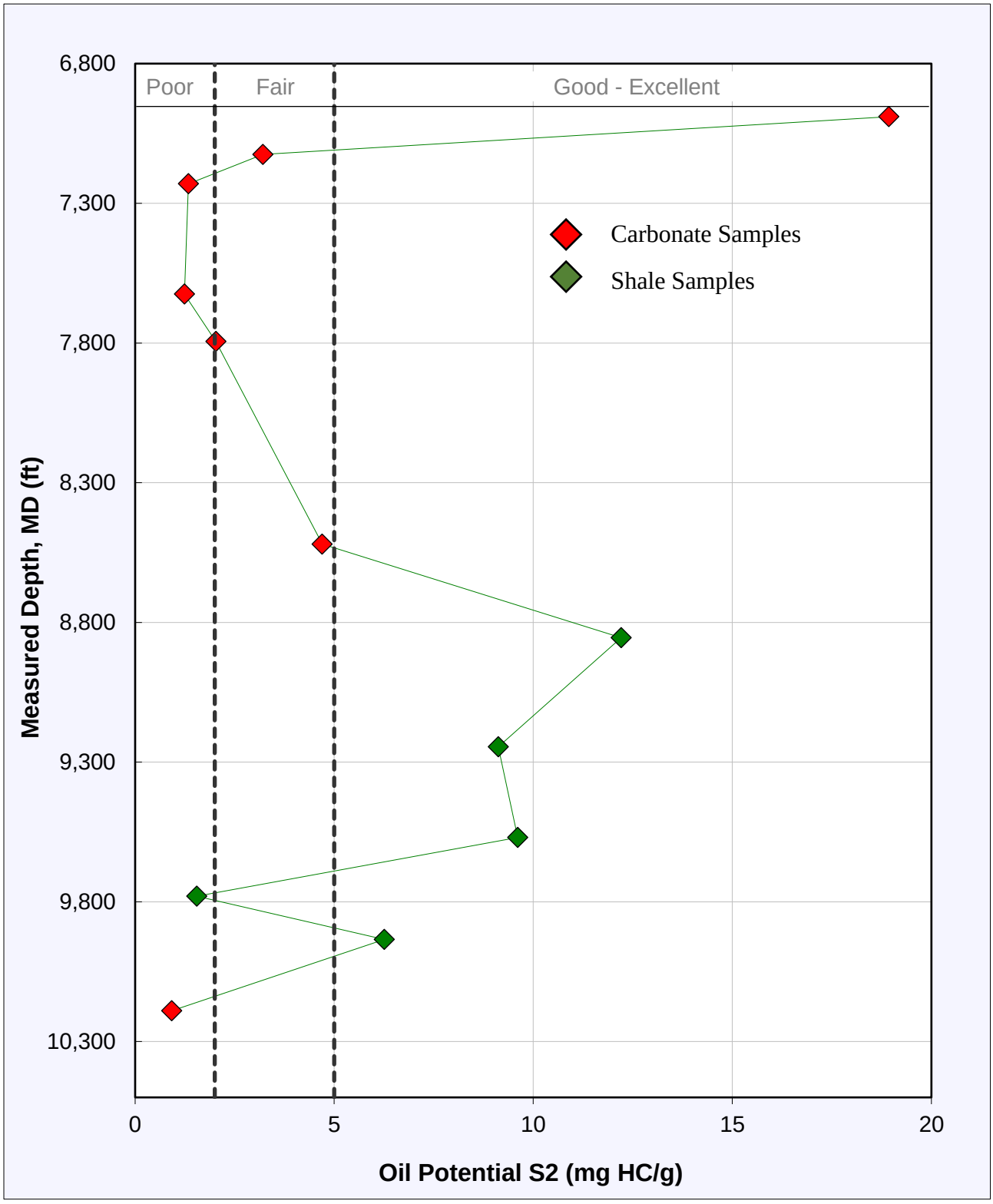

Figure 14: Oil potential S2 results as a function of sample depths

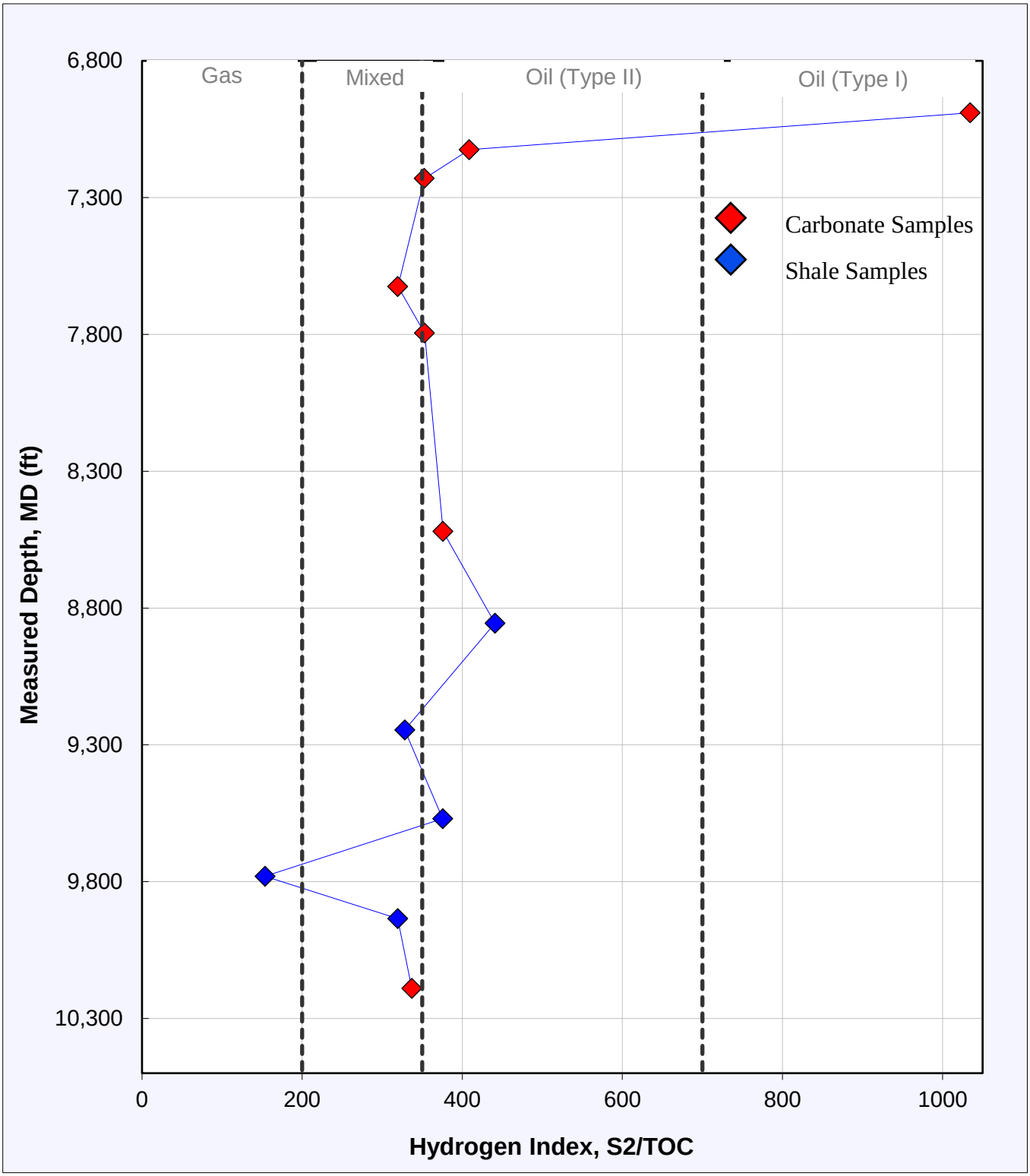

Figure 15: Hydrogen index results as a function of sample depths

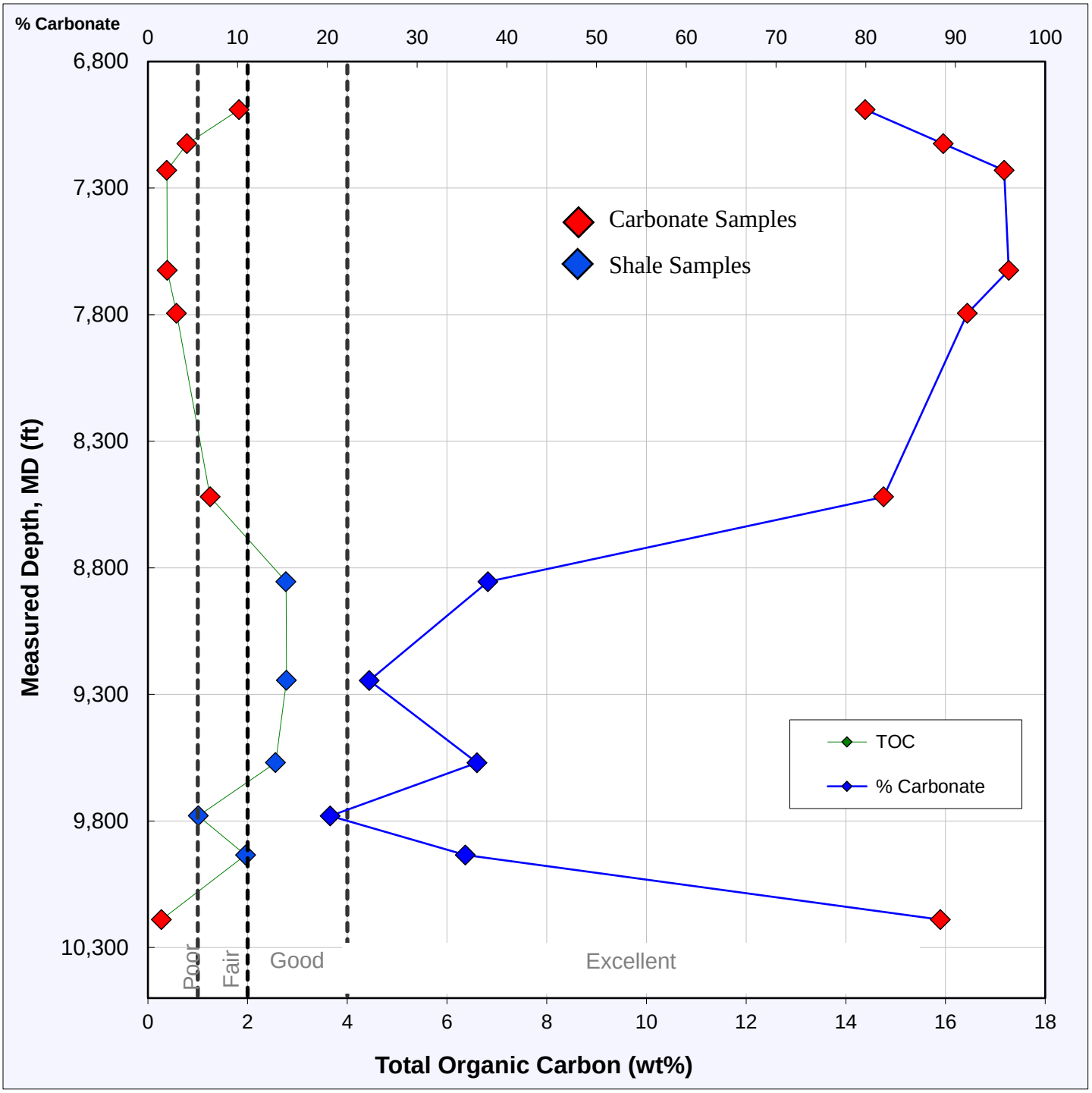

Figure 16: TOC and carbonate weight percentages as a function of sample depths

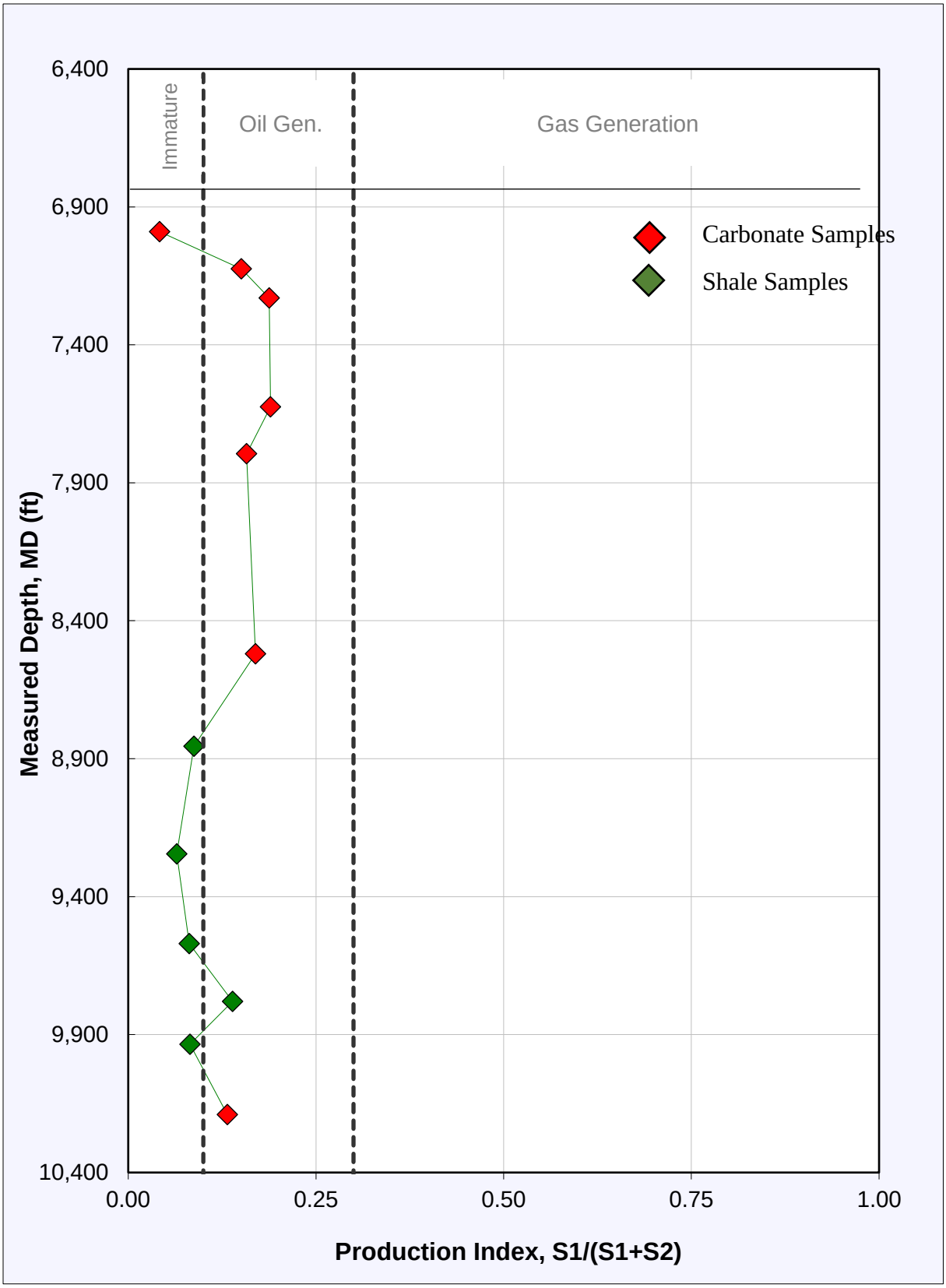

Figure 17: Production index results as a function of sample depths

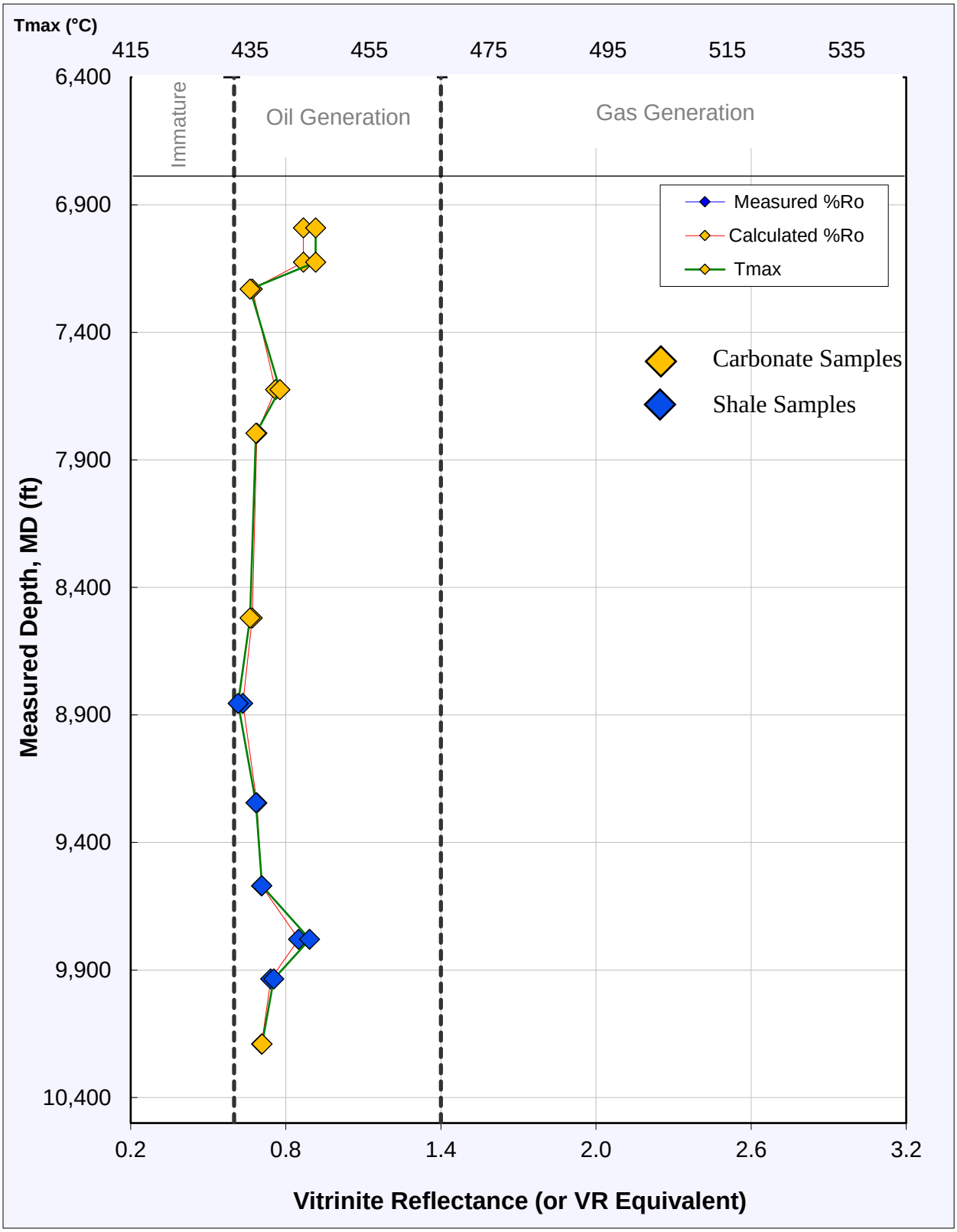

Figure 18: Vitrinite reflectance as a function of sample depths

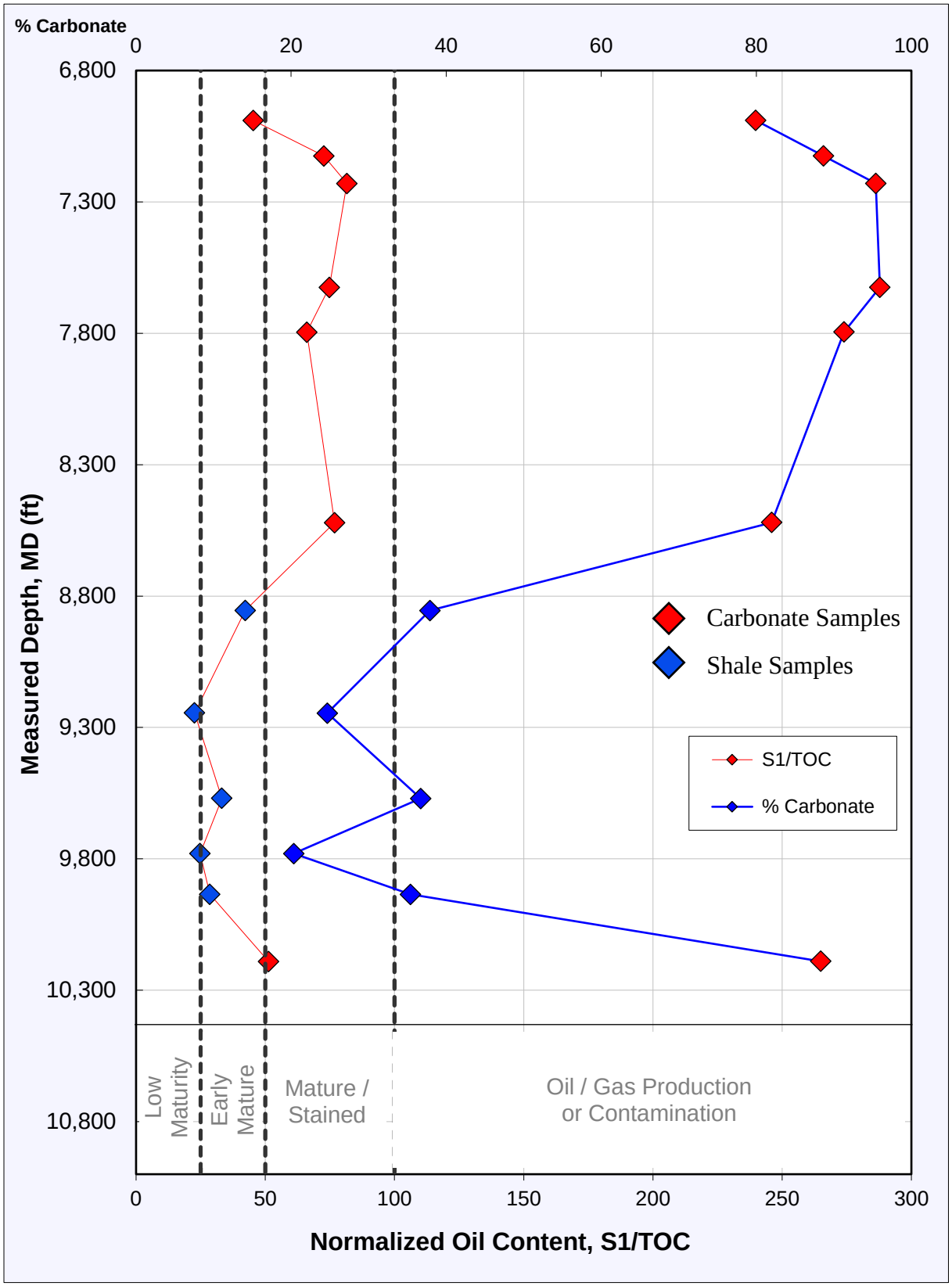

Figure 19: Normalized oil content compared to carbonate weight percentage and sample depths

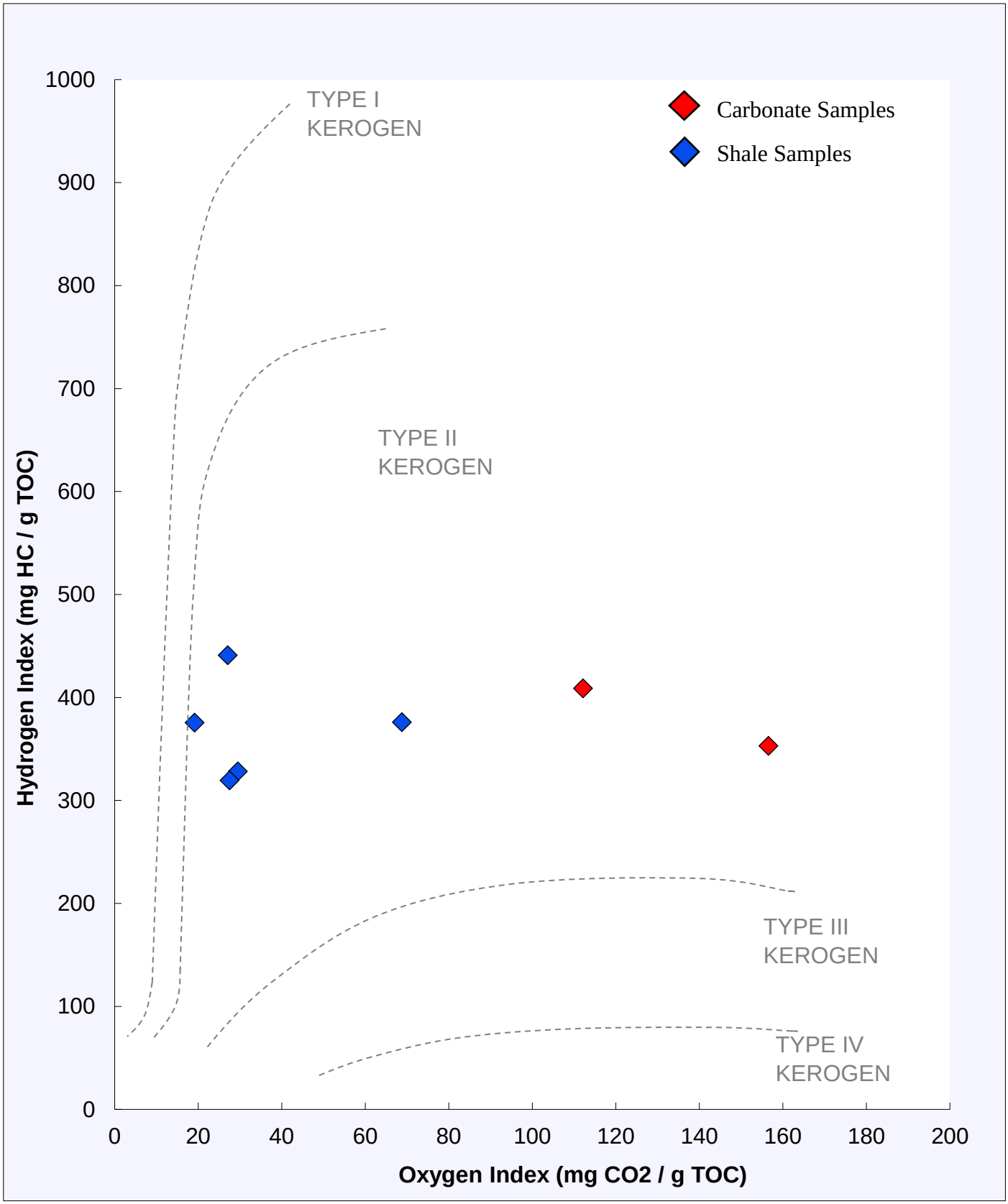

Figure 20: Pseudo Van Krevelen plot showing Oxygen Index vs. Hydrogen index for kerogen types

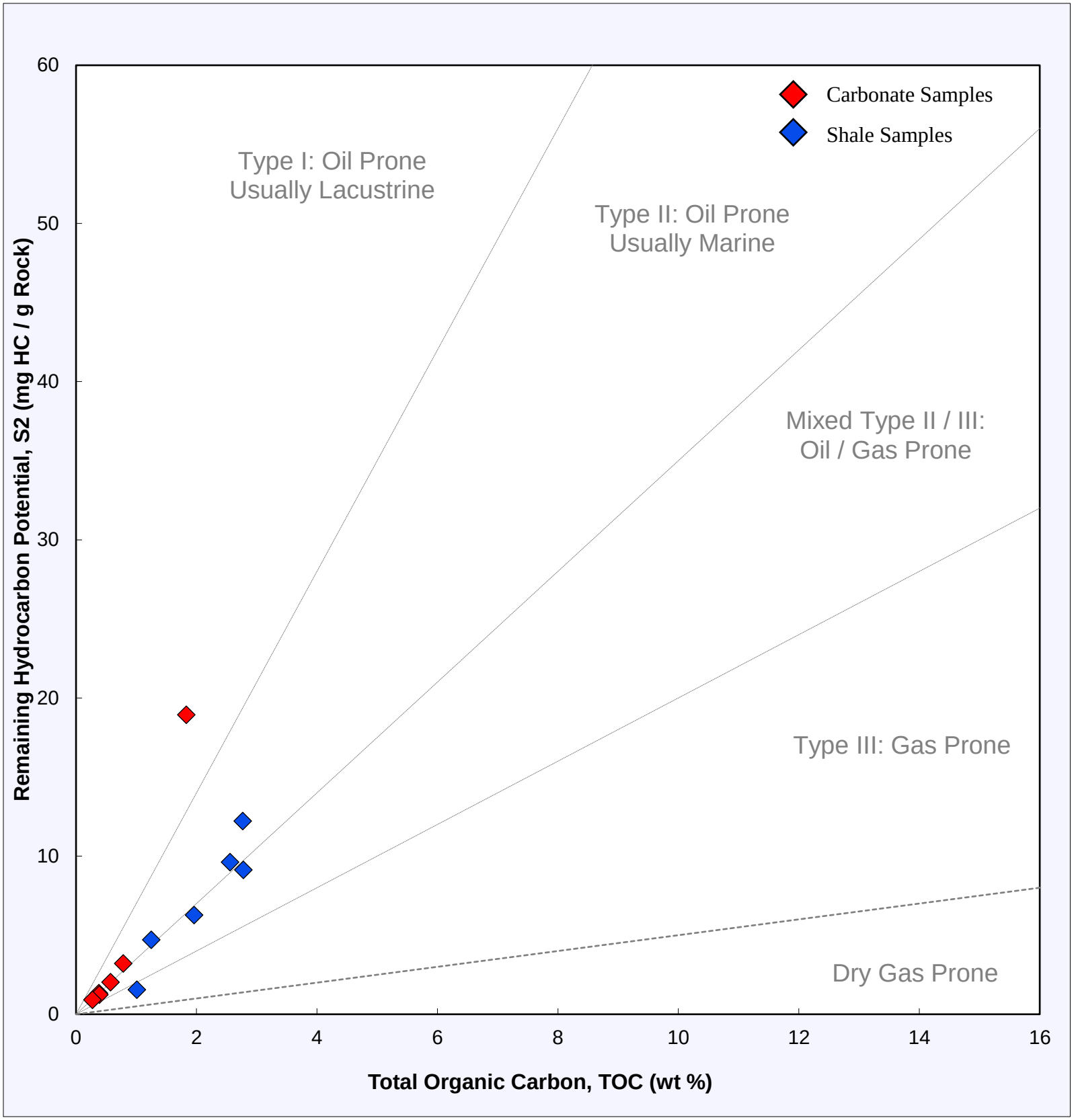

Figure 21: Kerogen quality plot of TOC vs S2

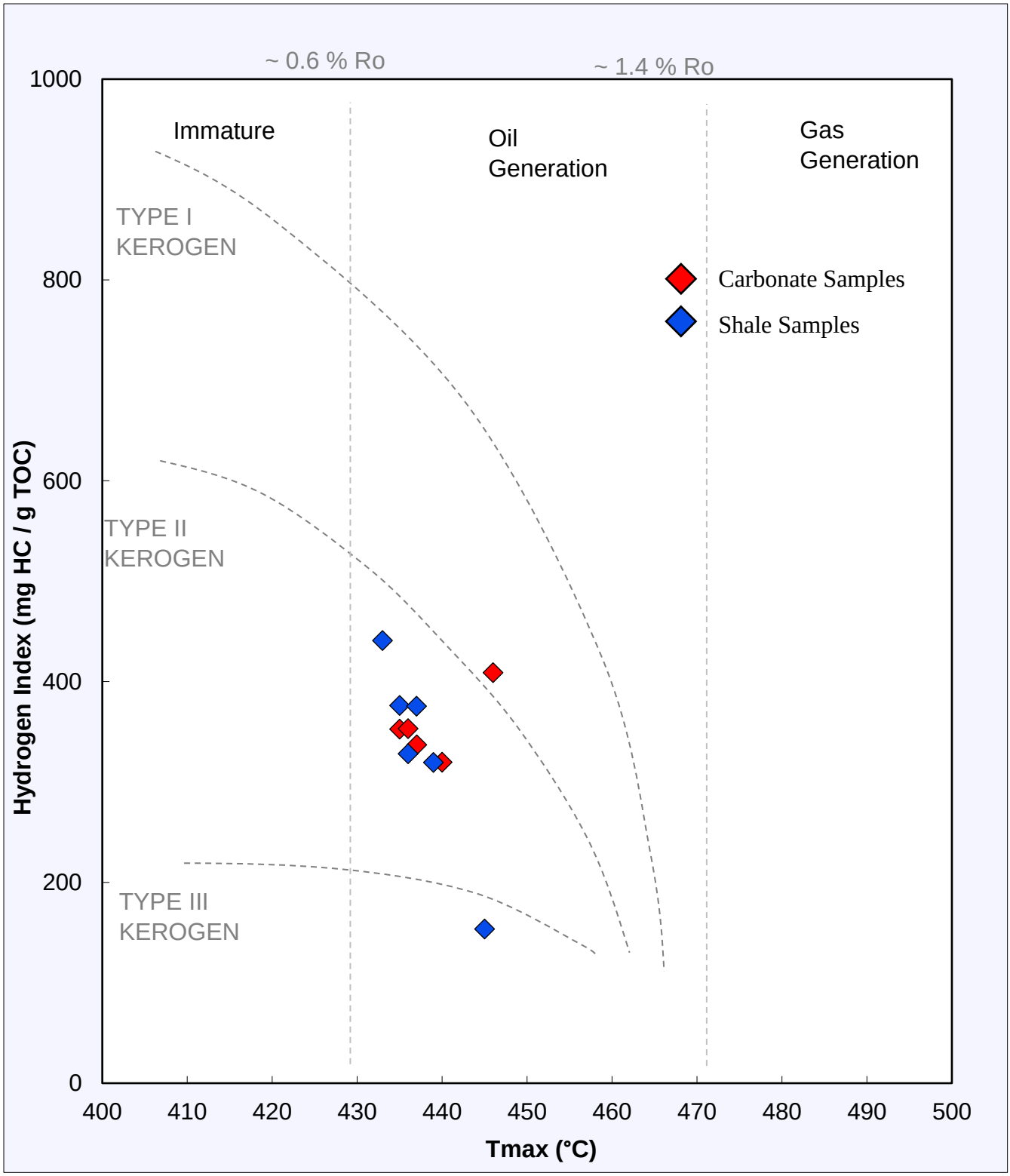

Figure 22: Kerogen type and maturity plot for T_{max} vs hydrogen index

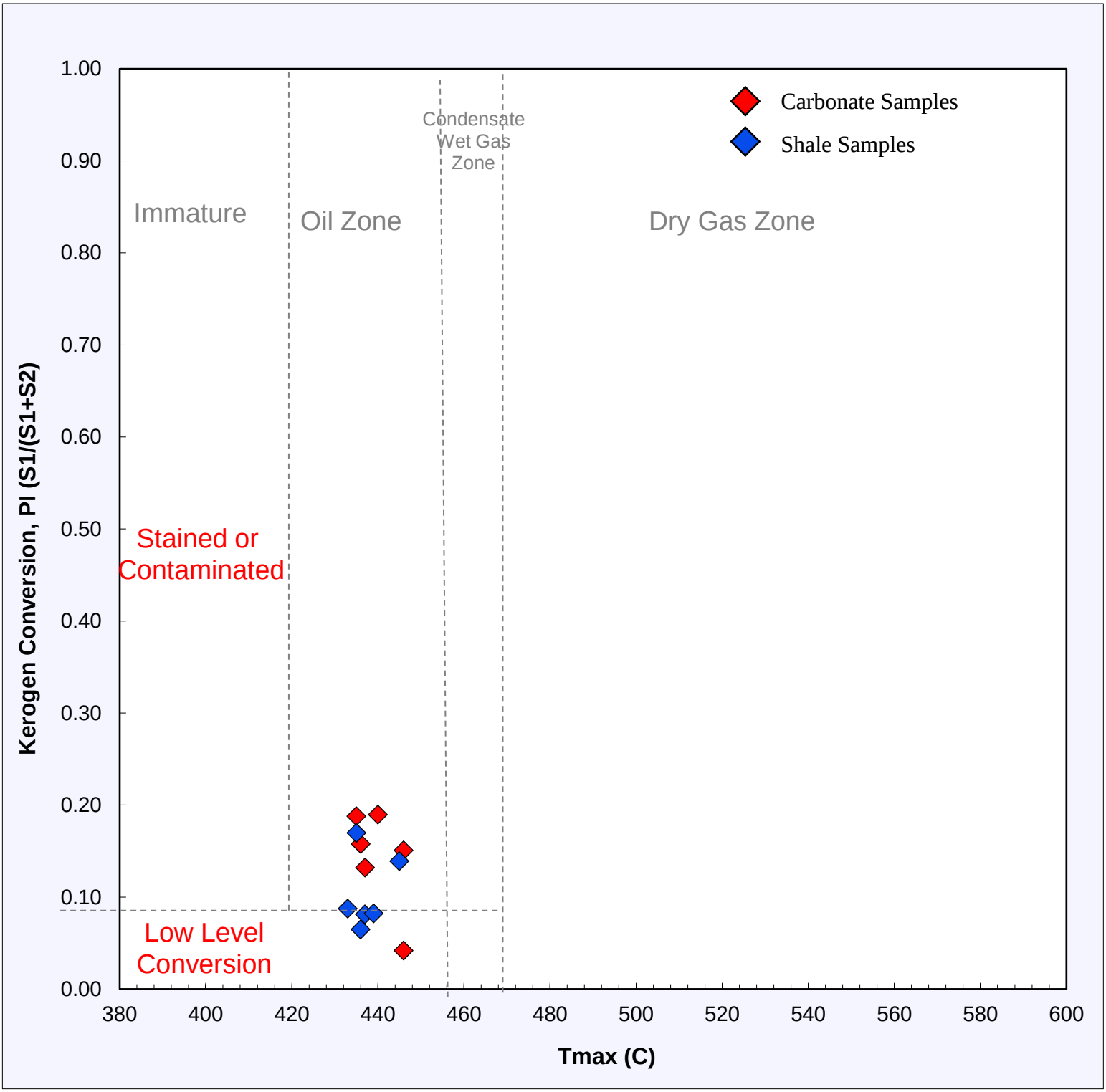

Figure 23: Kerogen conversion and maturity plot of T_{max} vs. PI

4.5 Gas Diffusion

Only Size B sample was run for the gas diffusion tests, as it has the largest sample mass from the grain size distribution of well cutting samples (Table 3). All diffusion coefficient results from the gas diffusion tests are shown in Table 8. Figure 24 shows an example of the raw data from Sample SK-1. Figure 25 shows an example from Sample SK-1 about how the effective diffusion coefficients (D_e) were derived using a $Ln[(C_t-C_i)/(C_0-C_i)$ processing (translation) of the O_2 signal results. Figure 25 then shows all the $Ln[(C_t-C_i)/(C_0-C_i)$ translated plots, including a Size B solid quartz control sample that is represented by the red dots.

Table 8: Test results of effective coefficients of diffusion (D_e, m^2/s)

Sample	D_e 1	D_e 2	D_e 3	Average ± standard deviation
SK-1	1.21E-05	2.04E-05	4.14E-05	2.46E-05
SK-2	9.84E-06	1.77E-05	4.40E-05	2.38E-05
SK-3	1.13E-05	1.82E-05	3.48E-05	2.15E-05
SK-4	1.09E-05	1.67E-05	3.25E-05	2.00E-05
SK-5	8.43E-06	1.66E-05	2.67E-05	1.72E-05
SK-6	1.08E-05	1.64E-05	3.21E-05	1.98E-05
SK-7	9.04E-06	1.62E-05	3.74E-05	2.09E-05
SK-8	1.08E-05	1.65E-05	3.23E-05	1.99E-05
SK-9	8.19E-06	1.12E-05	1.79E-05	1.24E-05
SK-10	1.25E-05	1.98E-05	3.31E-05	2.18E-05
SK-11	1.29E-05	2.59E-05	4.47E-05	2.78E-05
SK-12	9.48E-06	2.05E-05	3.66E-05	2.22E-05
Quartz B	1.02E-05	1.79E-05	3.08E-05	1.96E-05

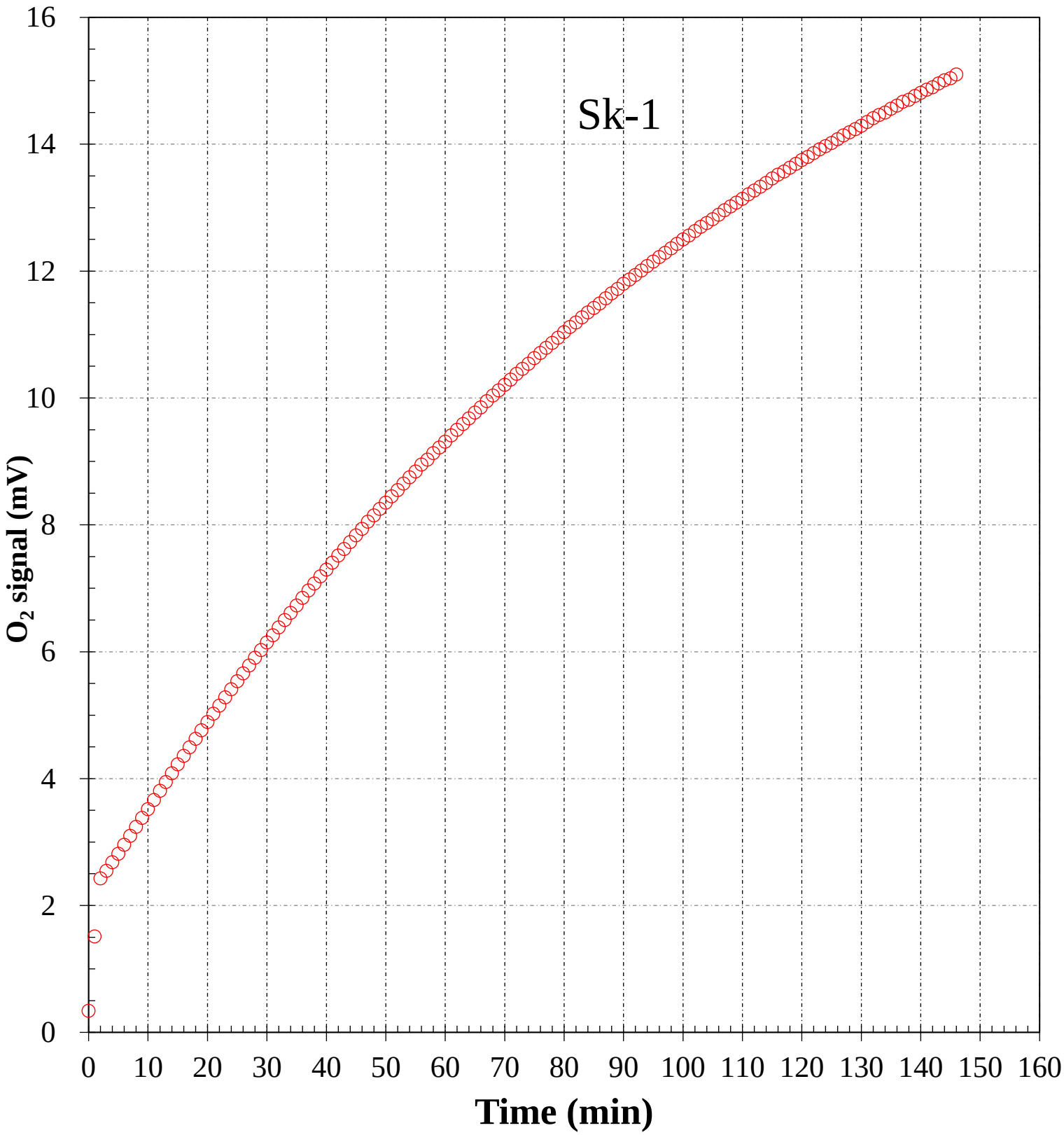

Figure 24: Example of raw data of gas diffusion tests for Sample Sk-1

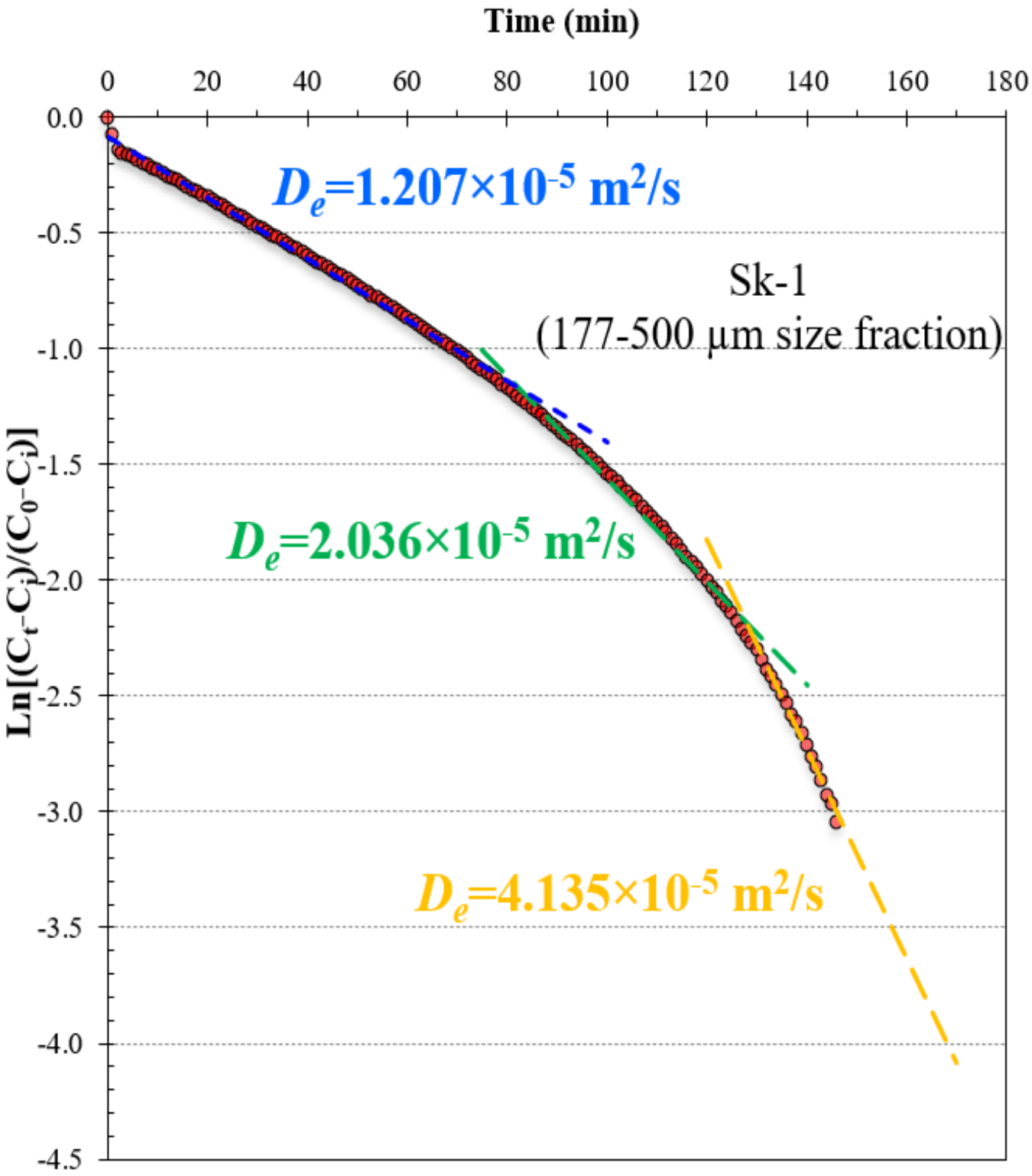

Figure 25: Example of $Ln[(C_t-C_i)/(C_0-C_i)$ plot to show how gas diffusion values (D_e) were derived from the experimental tests

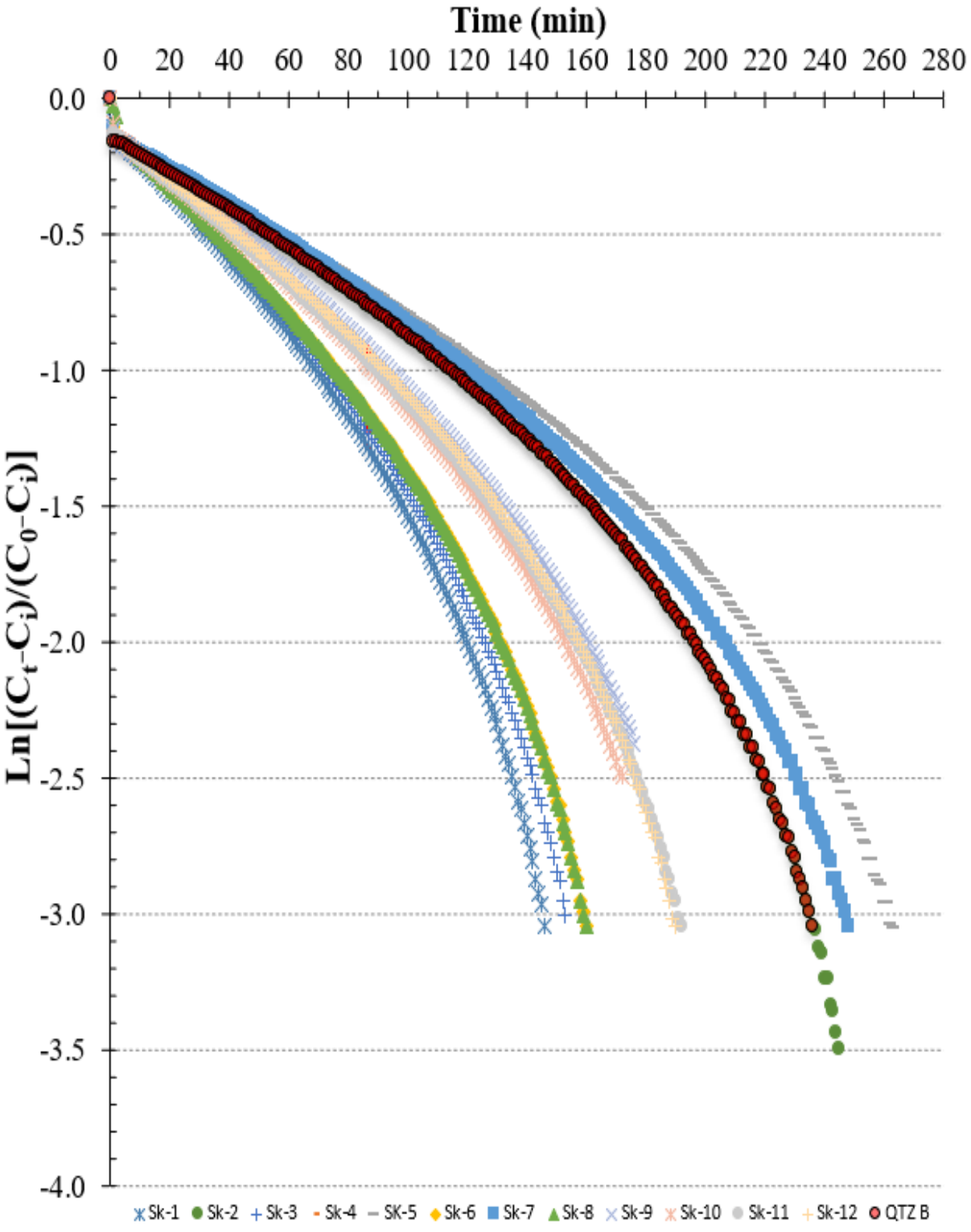

Figure 26: All Ln[(C_t-C_i)/(C_0-C_i) plots from gas diffusion tests with a B sized quartz control sample represented by the red dots

4.6 Porosity

All porosity results gathered by using bulk and particle densities are presented in Table 9, and these results are also illustrated by sample size in Figure 27.

Table 9: Results of porosity for three granular sizes

Sample	A	GRI	B
Sk-1	32.0%	23.9%	19.6%
Sk-2	22.9%	26.3%	21.6%
Sk-3	21.0%	19.7%	17.4%
Sk-4	15.3%	19.7%	13.3%
Sk-5	15.6%	20.4%	15.5%
Sk-6	15.3%	21.0%	24.1%
Sk-7	20.5%	6.9%	15.9%
Sk-8	20.3%	7.7%	20.6%
Sk-9	21.0%	9.0%	22.6%
Sk-10	16.9%	0.3%	18.4%
Sk-11	16.4%	7.2%	15.8%
Sk-12	19.8%	1.3%	27.3%

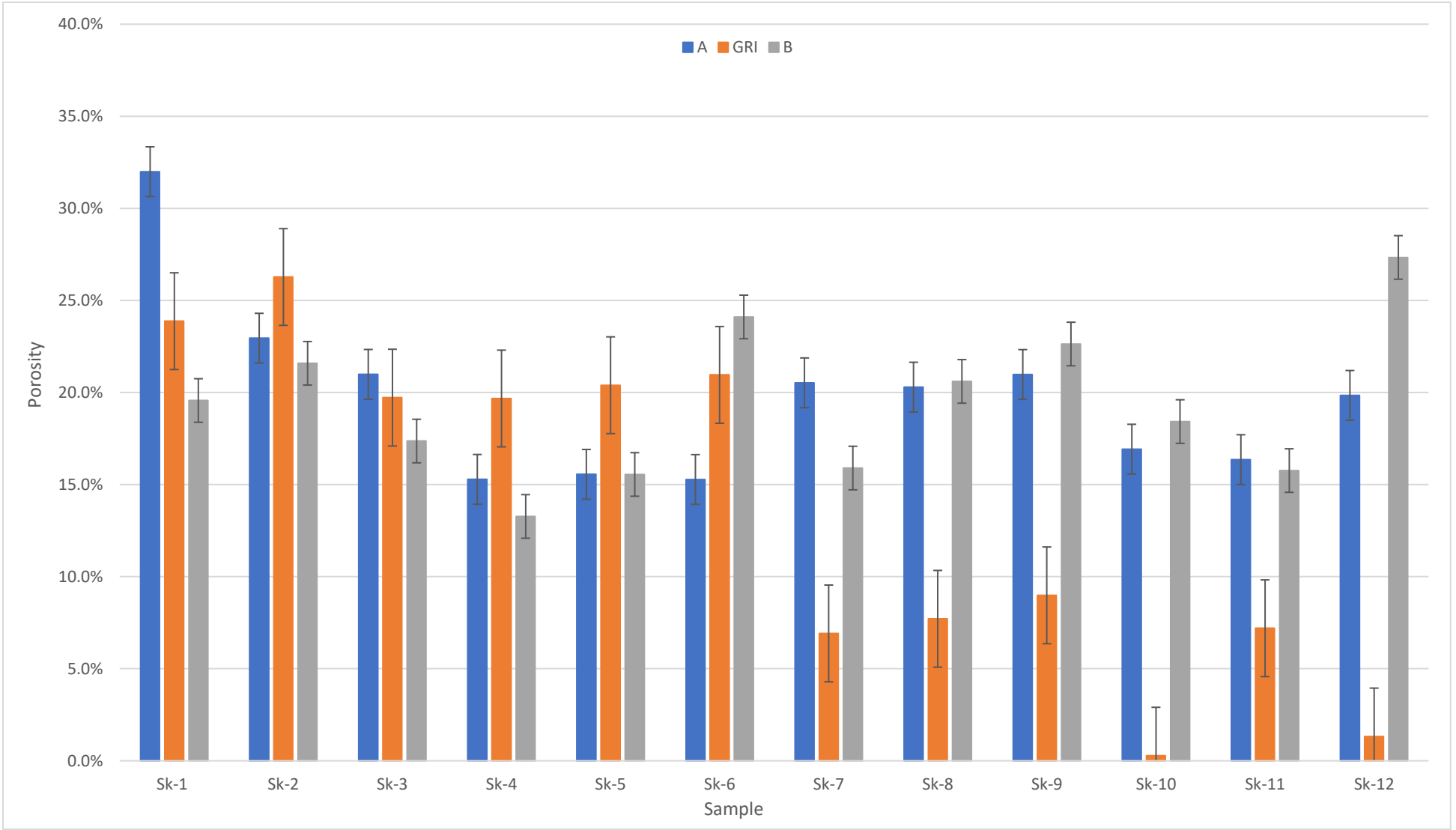

Figure 27: All porosity results by sample sizes with error bars

Chapter 5: Discussion

5.1 Particle Density

The particle density data show that Sample Sk-1 has the highest density among Size A samples at 2.915 g/cm^3. Sample Sk-10 has the highest density among GRI-sized samples at 2.739 g/cm^3 and is closely followed by Sk-12 at 2.738 g/cm^3. Sample Sk-10 also has the highest density among Size B samples at 2.743 g/cm^3. For Size C samples, Sk-4 has the highest density at 2.749 g/cm^3. All samples except for Sk-1, 10, and 12 show a slight increase of particle density between Sizes A and C. This slight density increase with the decreasing sample size is explained by the opening of isolated pore space which would make the samples slightly denser. The limestone samples also show a higher density due to higher percentages of dolomite and calcite minerals which are denser than the shale minerals. The general trends of particle density data match what is typically seen and expected from past studies such as Wang (2019) and Line (2020) that used core samples. This leads to the conclusion that well cutting samples are a viable substitution for core samples when running helium pycnometry to get particle density data.

The much larger particle density value for Size A of Sample Sk-1 could be an analytical error since this sample has a very limited mass of 0.3 g (Table 3). Therefore, the sample chamber was not completely full, which can lead to incorrect readings. Usually, 1 to 2 grams of samples were used for particle density measurement.

5.2 Bulk Density

Bulk density data show that Sample Sk-10 has the highest Size A density at 2.266 g/cm^3, and the highest size GRI density at 2.751 g/cm^3. Sample Sk-4 has the highest Size C density at 2.347 g/cm^3. Samples Sk-1 to-5 show an increase in bulk density between Sizes A and B. Samples Sk-7 to -12 have a relatively large increase in the bulk density in Size GRI samples. Just looking between sizes, Sizes A and B for samples Sk-7, 8, and 11 also have an increase in density as sample sizes get smaller. This again could be explained by the opening of isolated pore space with a decreasing sample size, leading to slightly higher densities. Size A samples were run using the DryFlo^{TM} method, and other sample sizes GRI and B were run using the quartz powder method. Size C samples were not run through bulk density due to their limited sample mass (Table 3). Samples Sk-7 through Sk-11 are all shale samples, showing a much higher bulk density for GRI sizes. The limestone samples Sk-1 through Sk-6 do not show this jump in Size GRI density. Sample Sk-2, 4, and 5 have their lowest bulk densities seen in the Size GRI samples.

When looking back at past works, the thesis of Becker (2019) presented the same trends in bulk density data as seen in this study. Becker's Wolfcamp A Formation samples show a decrease in bulk density from Size A samples to Size GRI samples and then another decrease in density from Sizes GRI to B samples. This trend is seen in samples ME 8621, ME 8633, ST 9733, ST 9841, and JB 9891 of Becker (2019). This same trend is observed in this study for Sample SK-6 which is from the Wolfcamp Formation from the well logs. The work of Becker (2019) showed that the Wolfcamp Formation in four parts A, B, C, and D, and Wolfcamp D is the same formation as the Cisco Formation. By looking at general depths of the samples to compare the thickness and composition of formation unites between two sampling locations, it

shows that Wolfcamp A from Becker (2019) matches up with what is called Wolfcamp on this study. It also appears that the Formation Wolfcamp Shale in this study relates to Wolfcamp B and C of Becker (2019). Lastly, it is apparent that the Cisco formation in this work is the same formation as the Wolfcamp D/ Cisco Formation of Becker (2019). Samples ME 9031, ST 9841, and JB 9891 from Becker (2019) are from the Wolfcamp B formation, and they show an increase in bulk density from Size A samples to Size GRI samples, and then a decrease in Bulk density from size GRI samples to Size B samples. Both thesis work of Jones (2019) and Mowery (2019) also show similar bulk density trends in Wolfcamp A samples as seen in this work and in Becker (2019).

All three thesis (Becker, 2019; Jones, 2019; Mowry, 2019) used core samples that were then crushed down to the granular sizes mentioned. The similarities in bulk density trends supports the idea that the core cuttings used in this work are a viable option when running the tests of this petrophysical property.

The Size A shale samples (Sk-7 to -11) were also run using the quartz powder method to ensure that there were no discrepancies between the DryFlo^{TM} and quartz-powder methodologies. There was a slight difference in the data as all the quartz-powder method results showed slightly higher densities than the DryFlo^{TM} results of the same sample. However, all the samples still showed the same trends as previously discussed with the Size GRI being denser and Size B being less dense.

5.3 X-Ray Diffraction

XRD data shows that shale samples have higher quartz and feldspar compositions than the carbonate samples, as expected. The data also show that the shale samples have a high

composition of clay minerals which is also to be expected. When looking at sample compositions from each formation used in this study it is seen that the data resemble that of past works. The only outlier is the amount of ankerite observed in a few samples is this study, which will be explained later.

The data show that first Wolfcamp sample (Sk-6) in this study is made up of over 80% carbonate minerals and about 13% of quartz/feldspar. This Wolfcamp sample as previously discussed can be related to the Wolfcamp A samples of past works. When looking at the trends in composition, it is seen that Sk-6 fits with trends of past data. For example, the Mzee thesis in 2019 shows Wolfcamp A samples have a higher carbonate composition than quartz and feldspar. Mzee (2019) also showed Wolfcamp A samples with higher calcite than dolomite compositions, which is also observed in Sk-6 in this study. Mzee (2019) also showed clays and pyrite compositions that match up to what is seen in Sk-6. Also, Mzee (2019) presented higher quartz/feldspar and pyrite compositions in Wolfcamp B samples than Wolfcamp A samples. This trend is also seen in this study as Samples Sk-7 to -9 all have increased contents of quartz/feldspar and pyrite when compared to Sk-6. Samples Sk-7 to -9 can all be related to Wolfcamp B or C, as previously discussed. The thesis work of Becker (2019) also reported that samples of Wolfcamp A and Wolfcamp B to have compositions like Sk-6 to -9. Both of these theses used core samples that were then crushed down to powder size for XRD analyses.

When looking at the XRD data, three is more ankerite being observed that what is expected from past works. Ankerite is carbonate with several different compositions, with a form of Ca (Fe, Mg, Mn)(CO_3)$_2$. In this study, it is most reasonable that the form being picked up by the XRD is CaFe(CO_3)$_2$. This would match up with the presence of siderite ($FeCO_3$) in Sample Sk-10. Although other studies show the presence of pyrite, they do not typically show other iron

minerals, and if they do it is not at as high of a percentage as seen in this study. This could be due to sample contamination from the fluids used during drilling. Since the cuttings get mixed with the drilling fluid, there is a high chance that anything in the drilling fluid could be present in the cutting's samples. Higher iron compositions would be expected, since hematite (Fe_2O_3) is one of the principal minerals used in drilling fluids (Garrett, 1987). Since the XRD is used to gather mineralogic compositions, added elements like iron can give off signals of iron-rich minerals such as ankerite and siderite; in this case the added iron oxide shows up as iron carbonates due to the presence of other carbonate minerals. To avoid this, in future works instead of using the powder size portion of sample directly from the sample envelope, the largest grain size with the most mass should be crushed to powder and used for XRD analyses. Since the powder-sized sample is collected at the bottom of the pan it collects all the soluble impurities that are washed off from the larger grain sizes. Therefore, if a larger size is washed, used for experiments, and then crushed to powder for mineralogical and geochemical tests, the data should better represent the composition of sample in situ. With the sample preparation adjustments, XRD could be a viable experiment for well cutting samples.

5.4 Pyrolysis and Total Organic Carbon (TOC)

Looking at TOC and pyrolysis data, it is obvious that most of the samples are kerogen type 2 as shown in Figures 20-22. The only samples that are not type 2 kerogen are Samples Sk-1,2, and 10. SK-10 is in the type 3 kerogen zone as defined and Sk-2 is in the kerogen 1 zone. All samples are seen in the oil zone when looking at Figure 22. Wolfcamp samples SK-7 to 9 are all in the good-to-excellent range when looking at oil potential plot of Figure 14. Figure 20 shows normalized oil content which puts the Wolfcamp sample in the early mature zone. As

Figure 17 shows Samples Sk-7 to 9 as immature based on the production index. An inverse relationship between TOC percentage of whole and carbonate percentage of whole is depicted in Figure 16.

When referencing past works that used powder sample derived from cores, Wolfcamp sample typically are classified as kerogen type 2 which matches the data received from this study using core cuttings. TOC values from past works are also constant with the values found in this study. In addition, the samples from this study match up with trends seen in previous works when comparing samples from the Wolfcamp formations. These similarities help uphold the idea the pyrolysis and TOC are viable method to use when characterizing well cuttings samples. TOC and pyrolysis results would also benefit from the sample preparation changes discussed for XRD.

5.5 Gas Diffusion

Based on Size B samples, the gas diffusion data show inconclusive results. To start there are three distinct groups when looking at Figure 27. The group on the right all have diffusion coefficients that are all about the same. All the samples that fall in this group on the right as ran in the same sample holder. When running the gas diffusion experiment there are two chambers to increase the testing efficiency, two sample holders were used both which have the same interior dimension, but one is 3 cm tall while the other 4 cm tall. The samples that plot in the group on the right side in Figure 27 were all placed in the 4 cm tall sample holder for analyses. These samples present a slower initial diffusion rate as the oxygen took longer to get through into the sensor chamber due to the added 1 cm sample height that it had to travel. This should have been adjusted for in the data reduction for D_e calculations but seems to have not been completely accounted for.

The larger issues that the gas diffusion data face is since the quartz control sample shows diffusion curve and effective diffusion coefficient almost similar to, but consistently smaller than, many of the samples. The quartz control sample was also analyzed in the 4 cm tall samples holder and can be seen in Figure 27 being represented as the red dots. The quartz control data plot exactly over the Sk-2 data, showing little variation from other samples that were analyzed in the 4 cm chamber. This should not be the case, as the quartz sample was used as a control due to it being non-porous within grains. When assuming that the quartz sample is non-porous it is expected that it will have the lowest diffusion rate, and this was not what is displayed. The other samples run in the 4 cm chamber like the quartz sample show a slower rate of diffusion than the quartz sample.

The data of gas diffusion test were all ran on Size B samples. Since the non-porous quartz sample and the test samples, with up to 27% porosity at the Size B level, show similar, if not the same, D_e values. This leads to the assumption that the gas does not diffuse through the pore space of the samples but rather though the interparticle pores since they are more accessible. These interparticle pores are the space between each grain of sample, meaning the gas does not travel through the sample grains but around them since it was more accessible in this experimental setup.

With the data from the gas diffusion test being inconclusive, the experimental method still needs to be adjusted to get conclusive data when running grain-sized samples or the method is simply not viable for granular samples as it is currently set up. This would make this experimental method not suitable for well cutting samples at this moment. It is possible that there was a large amount of leakage into the sample chamber as the quartz control also showed a nonlinear diffusion which is unexpected. Leakage tests were done but it is apparent that there

was still leakage since many other tests with the same gas diffusion set up typically show a linear diffusion for quartz samples. Overall, more testing is need before using gas diffusion for well cuttings.

5.6 Porosity

Porosity data were collected from the two-density method of bulk and particle density. Both methods are seen to be viable options when looking into the densities of well cutting samples, as the data received from this study showed similar results to data of studies that used core samples. To go even further, data from other studies that were able to run MIP tests show porosities in the same range as this study when looking at the GRI-sized samples of the Wolfcamp formation. To better investigate this similarity, samples from this study would need to be run through MIP and/or other methods such as nuclear magnetic resonance (NMR), but the data received from the two-density method is a good initial indicator that the methodology used in this work is valid.

Chapter 6: Conclusions and Future works

6.1 Conclusions

Overall, using well cuttings are shown to work for the analyses of petrophysical and geochemical properties in all used methodologies except for gas diffusion. Particle and bulk density methodologies do not require any changes. The XRD analytical process does not need to change; however, sample preparation for XRD needs to change, and a better understanding of drilling fluid would be helpful. TOC and pyrolysis are viable methods for characterizing well cuttings as they are; nevertheless, they could also benefit from the sample preparation changes that are needed for XRD. Lastly, porosity data received from the two-density methodology is viable for well cutting samples.

6.2 Suggestions

For future research, it would be advisable to run samples through MIP and NMR to make sure that data are congruent with past works performed on cores, as a versatile and complementary characterization tool. It would also be worth investigating samples with depth intervals that are completely continuous to better observe vertical trends. To do so, samples would have mixed lithologies, but will be able to show better characterizations of a vertical profile. This study had gaps between sample intervals to make sure that lithologies of samples were consistent (all shale or all limestone). These gaps made it difficult to see any vertical trends. Therefore, the next steps should be to investigate the Dean Formation interval from the Spade K well. These samples were left out of this study due to having a mixed lithologies. Samples from the Dean formation will demonstrate the validity of these methodologies when using samples of mixed lithologies. Another issue that this study had, making vertical trends hard to identity, lies

in the limited number of samples (only 1-5 samples per formation). Therefore, it is recommended that more well cutting samples be collected if future studies were to be carried out to investigate vertical trends. Lastly, if possible, more mass of cuttings would help; for example, if each 10-foot interval envelope could have 10 g of sample instead of 5 g, this would allow sample intervals to be smaller and more test to be run, which will better show vertical trends.

REFERENCES

Ahmed, K., Lower, P., Graham, K., Merkel, D. 2020. A More Accurate Integrated Multimineral Petrophysical Model in Unconventional Reservoirs using Data from Cuttings: A Case Study from Powder River Basin, USA. Unconventional Resources Technology Conference (URTeC) DOI 10.15530/urtec-2020-2888

Beaumont, C. 1981. Foreland basins, Geophysical Journal of the Royal Astronomical Society, v. 65, p. 291 -329.

Becker, S.J. 2019. Laboratory-scale petrophysical evaluation of lithofacies effect on reservoir & source quality and core-calibrated well log analysis in Pennsylvanian-Permian Wolfcamp-Spraberry intervals, Midland Basin, Texas, USA. Master's Thesis, the University of Texas at Arlington.

Brown, L. F., J. R. Cleaves, A.W. Erxleben. 1973. Pennsylvanian depositional systems in North-Central Texas, a guide for interpreting terrigenous elastic facies in a cratonic basin. The University of Texas at Austin, Bureau of Economic Geology, Guidebook 14, 122 pp.

Carreno, A.M., M.R. Perez, N. Marfisi, J.J. Gomez, E.R. Perez. 2018. Integrated Methodology for Laboratory Evaluation of Shale Plays Cuttings: SPE-19191818-MS ttps://www-onepetro-org.ezproxy.uta.edu/download/conference-paper/SPE-191812-MS?id=conference-paper%2FSPE-191812-MS

Garrett, R.L. 1987. Quality requirement for industrial minerals used in drilling fluids. *Journal of Mineral Engineering*, 39:11. https://www.osti.gov/biblio/5755997-quality-requirements-industrial-minerals-used-drilling-fluids

Ghosh, W.K., S.F. Urschel, G.M. Friedman, 1985. Substitution of Simulated Well-Cuttings for Core-Plugs in the Determination of Petrophysical Properties for the Use in Reservoir Analyses https://www-onepetro-org.ezproxy.uta.edu/download/general/SPE-14704-MS?id=general%2FSPE-14704-MS

Jones, R. 2019. Nanopetrophysical Characterization of the Wolfcamp A Shale Formation in the Permian Basin of Southeastern New Mexico, U.S.A. Master's Thesis, the University of Texas at Arlington.

Jordan, T. E. 1981. Thrust loads and foreland basin development, Cretaceous western United States. AAPG Bulletin, 11, 65, p. 2506-2520.

Mowery, B. 2019. Nano-petrophysical study of the Dean, Wolfcamp, and Canyon formations of the Midland Basin, Texas, USA. UTA.

Mzee, N. 2019. Nano-petrophysics of the Dean, Spraberry, and Wolfcamp formations of the Midland Basin. Master's Thesis, the University of Texas at Arlington.

Peng, S., Q.H. Hu, and S. Hamamoto. 2012. Diffusivity of rocks: Gas diffusion measurements and correlation to porosity and pore-size distribution. *Water Resources Research*, Vol. 48, No. 2, W02507.

Permata, I., S. Khakimov, S. Kenzhekhanov, M. Toktarov, K. Clippinger. 2020. Terra Laboratories. Colorado School of Mines. High Resolution Cuttings Analysis for Well Placement in the Uinta Basin. 2020, Unconventional Resources Technology Conference (URTeC) DOI 10.15530/urtec-2020-3118.

Robinson, K. 1988. Petroleum geology and hydrocarbon plays of the Permian Basin Petroleum province West Texas and southeast New Mexico, U.S. Geological Survey Open-File Report 88-450-Z, 53 pp.

Santarelli, F.J., A.F. Marsala, M. Brignoli, E. Rossi, N. Bona. 2000. SpA Formation Evaluation From Logging on Cuttings https://www-onepetroorg.ezproxy.uta.edu/download/journal-paper/SPE-36851-PA?id=journal-paper%2FSPE-36851-PA.

US DOE, EIA. "Permian Basin." *Eia.gov*, U.S Energy Information Administration, Oct. 2018, www.eia.gov/maps/pdf/PermianBasin_Wolfcamp_EIAReport_Oct2018.pdf.

US DOE, EIA. "Permian Basin Part 2." *Eia.gov*, U.S Energy Information Administration, Aug. 2020, www.eia.gov/maps/pdf/Permian_Wolfcamp_Midland_EIA_reportII.pdf.

Wittman, B., M. Hemenway, D. Michael, D. Veselinovic, T. Kenney, D. Green, H. Rowe. 2020. Integration of Geochemical and Petrophysical Measurements from Drill Cuttings for Unconventional Reservoir Characterization, Converse County, Powder River Basin. 2020, Unconventional Resources Technology Conference (URTeC), URTeC 3290

Wang, Q. 2019. Nano-petrophysics study of Haynesville Shale, East Texas, USA. Master's Thesis, the University of Texas at Arlington.

Yang, K.M., and S. Dorobek. 1995. The Permian Basin of West Texas and New Mexico: Tectonic history of a "composite" foreland basin and its effects of stratigraphic development, Texas A&M. pp. 149-174.

Zhao, C., W. Zhou, Q.H. Hu, H. Xu, T. Zhang, and C. Zhang. 2021. Porosity measurement of granular rock samples by modified bulk density analyses with particle envelopment. *Marine and Petroleum Geology*, 133, 105273. DOI: 10.1016/j.marpetgeo.2021.105273.

Appendix A

Laboratory Methods for XRD Analyses at the Shimadzu Center, The University of Texas at Arlington

MaximaX XRD-7000: Shimadzu X-Ray Diffractometer

Sample Preparation

- Prepare your sample by compacting the sample into the sample holder using a glass slide.
- Avoid vertical loading by removing excess sample with the edge of the glass slide.
- Attempt to make your sample as flat and homogenous as possible; once this is completed your sample is ready to be analyzed.

Powder Operations

- Turn the chiller on by pressing the power button (on the face of the chiller), a green light will illuminate.
    - Allow the chiller to sit for ~20 minutes to adjust to the proper temperature.
- Turn the XRD on by pressing the power button on the left hand side. The green power button will illuminate on the front panel of the XRD.

XRD calibration:

- Locate and open the [PCXRD] program on the desktop. The main "XRD-6100/7000" panel will display.
- Click the [Display and Setup] icon, a "door alarm check" window will pop up. Follow the prompt to open and close the XRD door, once complete click "Close". An "IOcon" window will pop up with the message "Now Calibration! If ready OK", Click "OK".
- The XRD is officially calibrated and ready to process your sample.

Setting Analysis Conditions:

- To set the processing conditions go to the "XRD 6100/7000" panel.
- Click on the [Right Gonio Condition] icon to open the [Analysis Condition Edit Program] window.
- Click the blue bar under [Measurement Mode: Standard] to open the [Standard Condition Edit] window.
- Most of the settings in the [Standard Condition Edit] window will be preset. Only a few conditions will need to be changed.
- The following general condition settings will work for a wide array of materials.

  It's very important to follow these next steps, double check any settings you change ensuring to follow these guidelines precisely, this will minimize minor mistakes when processing materials and will prevent damage to the detector.

- Scanning condition: Scan Range (deg) = 2°-70° □ Optional Condition: Check the box [Option Enable]
- Beta Attachment: Control Mode: Rotation
  Rotation Speed (rpm): 6 ○ Slit Condition: Slit Conditions are preset and must be verified on the XRD to ensure the proper slit sizes match the setting listed under the Slit Conditions.
- Checking the Slits:
  - ✦ Open the XRD door, on the left side of the XRD is the X-ray tube, the Divergence Slit is attached to the left side of the divergence soller slits.
  - ✦ On the right hand side will be the detector arm which contains a set of Scattering soller slits, the Scattering Slit faces the sample (Left) and the Receiving Slit faces the detector (Right).
  - ✦ If they are not the same sizes as what is preset in the [Slit Condition] box change the slit's so the do match.
- ○ Standard Slit Settings:
  - ✦ Divergence Slit: 1.0°
  - ✦ Scattering Slit: 1.0°
  - ✦ Receiving Slit: 0.3 mm

- Double check your settings and make sure they are correct, if they are click [OK].
- A [File & Sample Condition Edit] window will display; change the [Group name] to match your destination folder name and change [File name] and [Sample Name] to match your sample name, click [New]. ○ Later samples can be created by simply changing the file and sample names and clicking [Modify].
- Click [Close] on the [Standard Condition Edit] window.

Starting the XRD Processing:

- Locate and click the [Right Giono Analysis] icon on the [XRD-6100/7000] panel.
- Your current sample name should appear highlighted blue in the upper portion of the [Right Gonio System: Analysis Condition Edit Program] window. Highlight your sample and click [Append], this adds your sample to the list in the bottom portion of the window labeled [Entry for Analysis], click [Start]. Your sample should appear in the bottom of the [Right Giono Analysis & Spooler Program] window, click [Start] in this window. This officially starts the analysis process.
  - Indicators for Analysis: A clicking sound will come from the XRD when the locking mechanism on the sliding door locks. On the face of the XRD a yellow light should illuminate under [X-RAYS ON].
- Leave all software windows open and allow the XRD to process your sample, this should take ~30 minutes.

Completed XRD Processing:

- A complete peak spectrum should appear in the [Right Giono Analysis & Spooler Program] window upon completion.
- The green [Analyzing!] Box should disappear and the yellow [X-RAYS ON] light should turn off.
- If you have more samples to analyze, continue to run your samples in the same manner listed above.

Opening Peak Profile Spectrum:

- Locate and open the icon for the [MDI jade 9] software on the Desktop.
- Under [File], click [Read], locate the folder [xddat] under [favorites]. Locate the folder where your samples are saved.
- In your folder, each sample should have a [.RAW] file, use this file to open your selected spectrum in the [Jade 9] software.

Identifying Minerals in Peak Spectrum:

It's important to have the educated background on the sample you're analyzing. Knowledge regarding the bulk composition and what you're searching for will greatly reduce the amount of time spent IDing the various peaks in the spectrum

- Locate the [Find Peaks] icon on the main tool bar next to the [Floppy Disk/Save] icon, this will identify and mark any statistically significant peaks within the spectrum.
- Choose a mineral database: At the top of the panel to the right of the spectrum window, there will be a drop-down menu choose the [RDB-Minerals] as the database. The RDB-Mineral database should be predominately used to identify most minerals in your spectra.
    - If you cannot find a mineral in the RDB-Minerals database change to the [PDF+4 Minerals] database library but be sure to change back to the RDB database once the mineral is located.
- Begin searching for minerals based on your pre-existing knowledge regarding the sample. When you identify minerals that fit your peak spectrum hit [Enter] on the keyboard, this process will add the minerals to ta compiled list of those minerals which you identified in the spectrum.
- Once you have exhausted your initial hypothetical list of minerals, a helpful tool to use is the [Line Based Search/Match]. Go to the main tool bar and locate [Identify] and select the [Line Based Search] option.
    - This tool will compile a list of minerals by searching a selected PDF database for entries with peaks which are statistical matches for the peaks identified within your spectrum.
    - Settings:
        - ✦ [Two-Theta Error Window] max setting should be no more than 0.24%

✦ [Top Hits to List] max setting 80 ○ Set the parameters and click the blue [Play] icon next to the [X] to run the search and generate a list of possible phases that might fit your spectra. *Note: the line based search should not be used as a primary way to identify the bulk mineral mode of the sample as the software is not consistent when generating phases and will possibly leave out important phases for the spectrum*.

Model Analysis:

- Once all minerals have been ID'd, check that they have been added to the mineral list by pushing [Enter] on the keyboard.
- Click the [%] icon next to the drop-down mineral list located on the toolbar in the middle of the window to begin modal analysis.
    - An overlay will appear with different chart configurations of the modal results, to change the configurations of the chart use the drop-down menu in the chart window.
- To view the modal analysis in text format: locate and click the […] icon near the [%] icon. This will list the minerals by name, chemical formula, and the normalized weight percent for each mineral. It will also state if the mineral is [major], [minor], [trace], or [absent] component in the sample.
- If you would like to remove a mineral from your mineral list at any time, highlight the mineral and press [Delete] on the keyboard. [Absent] phases should be removed from the list by this method.

Analysis Check with Pattern Deconvolution:

- A key that the peak spectrum has been fully fitted and identified is by using the [Pattern Deconvolution] tool which automatically runs with the modal analysis. ○ The pattern deconvolution tool will generate a red overlay spectrum on top of the original white spectrum.
    - This process is generating a [Best Fit Profile] composed of the selected mineral standards from the [Mineral PDF database library] with your sample spectrum. ○ If all minerals have been properly identified, then the red deconvolution overlay will match the peak spectra for each peak. If there are peaks that don't have the red deconvolution overlay, then those peaks have not been identified.
- Continue processing your spectrum until your original spectra and the deconvolution spectra match.

Saving Data:

To save your data,

Go to [file] and [Save], save your data under [Current work as *.SAV]. This will save all analysis as a separate file.

Appendix B

Laboratory Methods for Total Organic Carbon and Pyrolysis Analyses at GeoMark Research

1. Sample Requirements for a Typical Geochemical Program

For geochemical analysis, a teaspoon (ca. 10 g.) of sample material is needed when TOC, RockEval, vitrinite reflectance and residual hydrocarbon fluid fingerprinting is to be completed. If possible, a tablespoon is preferred. However, it is possible to complete a detailed program with even less sample, although there is dependency on the sample characteristics (e.g., organic richness, abundance of vitrinite, amount of staining). Sample prep includes grinding the sample with mortar and pestle until it passes through a 60-mesh sieve. 2.

2.Total Organic Carbon (TOC) – LECO C230 instrument

Leco TOC analysis requires decarbonation of the rock sample by treatment with hydrochloric acid (HCl). This is done by treating the samples with Concentrated HCl for at least two hours. The samples are then rinsed with water and flushed through a filtration apparatus to remove the acid. The filter is then removed, placed into a LECO crucible and dried in a low temperature oven (110 C) for a minimum of 4 hours. Samples may also be weighed after this process in order to obtain carbonate% based on weight loss.

The LECO C230 instrument is calibrated with standards having known carbon contents. This is completed by combustion of these standards by heating to 1200°C in the presence of oxygen. Both carbon monoxide and carbon dioxide are generated, and the carbon monoxide is converted to carbon dioxide by a catalyst. The carbon dioxide is measured by an IR cell. Combustion of unknowns is then completed and the response of unknowns per mass unit is compared to that of the calibration standard, thereby the TOC is determined.

Standards are analyzed as unknowns every 10 samples to check the variation and calibration of the analysis. Random and selected reruns are done to verify the data. The acceptable standard deviation for TOC is 3% variation from established value.

3. Rock Eval / HAWK Pyrolysis

Approximately 100 mg of washed, ground (60 mesh) whole rock sample is analyzed in the Rock-Eval or HAWK instrument. Organic rich samples are analyzed at reduced weights whenever the S2 value exceeds 40.0 mg/g or TOC exceeds 7-8%. Samples must be reanalyzed at lower weights when these values are obtained at 100 mg.

RE-II Operating Conditions

S1: 300°C for 3 minutes

S2: 300°C to 550°C at 25°C/min; hold at 550°C for 1 minute

S3: trapped between 300 to 390°

RE-VI Operating Conditions

S1: 300°C for 3 minutes

S2: 300°C to 650°C at 25oC/min; hold at 650°C for 0 minute

S3: measured between 300 to 400°

HAWK Operating Conditions

S1:300°C for 3 minutes

S2: 300°C to 650°C at 25°C/min; hold at 650°C for 0 minute

S3: measured between 300 to 400°

Measurements from Rock-Eval are:

S1: free oil content (mg HC/g rock)

S2: remaining generation potential (mg HC/g rock) T_{max}: temperature at maximum evolution of S2 hydrocarbons (°C)

S3: organic carbon dioxide yield (mg CO2/ g rock)

Several useful ratios are also utilized from Rock-Eval and TOC data. These are:

Hydrogen Index (HI): S2/TOC × 100 (in mg HC/g TOC)

Oxygen Index (OI): S3/TOC × 100 (in mg CO2/g TOC)

Normalized Oil Content: S1/TOC × 100 (in mg HC/g TOC)

S2/S3: S2/S3 (in mg HC/CO2)

Production Index (PI): S1/ (S1+S2)

Instrument calibration is achieved using a rock standard. Its values were determined from a calibration curve to pure hydrocarbons of varying concentrations. This standard is analyzed every 10 samples as an unknown to check the instrument calibration. If the analysis of the 81 standards ran as an unknown does not meet specifications, those preceding data are rejected, the instrument recalibrated, and the samples analyzed again. However, normal variations in the standard are used to adjust any variation in the calibration response. The standard deviation is considered acceptable under the following guidelines:

T_{max}: +/- 2°C

S1: 10% variation from established value

S2: 10% variation from established value

S3: 20% variation from established value

Analytical data are checked selectively and randomly. Selected and random checks are completed on approximately 10% of the samples. A standard is analyzed as an unknown every 10 samples.

4. Turnaround Time:

The standard turnaround time for sample orders over the past 12 months is approximately 2 to 3 weeks, depending on number of samples in the order.